


RESEARCH

Open Access



# MST1, a novel therapeutic target for Alzheimer's disease, regulates mitochondrial homeostasis by mediating mitochondrial DNA transcription and the PI3K-Akt-ROS pathway

Dongqing Cui<sup>1</sup>, Haixia Liu<sup>1</sup>, Lili Cao<sup>2</sup>, Xiaowei Du<sup>3</sup>, Dingxin Liu<sup>3</sup>, Zhiping Liu<sup>4</sup>, Tong Wang<sup>4</sup>, Hui Yang<sup>1</sup>, Xiaolei Zheng<sup>1</sup>, Zhaohong Xie<sup>1</sup>, Shunliang Xu<sup>1</sup>, Jianzhong Bi<sup>1</sup> and Ping Wang<sup>1\*</sup> 

## Abstract

**Background** Alzheimer's disease (AD) is a prevalent irreversible neurodegenerative condition marked by gradual cognitive deterioration and neuronal loss. The mammalian Ste20-like kinase (MST1)–Hippo pathway is pivotal in regulating cell apoptosis, immune response, mitochondrial function, and oxidative stress. However, the association between MST1 and mitochondrial function in AD remains unknown. Therefore, this study investigates the effect of MST1 on neuronal damage and cognitive impairment by regulating mitochondrial homeostasis in AD.

**Methods** In this study, 4- and 7-month-old 5xFAD mice were selected to simulate the early and middle stages of AD, respectively; age-matched wild-type mice served as controls for comparative analysis. Adeno-associated virus (AAV) was injected into the hippocampus of mice. Four weeks post-injection, cognitive function, neuronal damage indicators, and mitochondrial morphology, dynamics, oxidative stress, ATP, and apoptosis-related indicators were evaluated. Additionally, RNA-sequencing was performed on the hippocampal tissue of 5xFAD mice and MST1-knockdown 5xFAD mice. Subsequently, Gene Ontology (GO) enrichment and Kyoto Encyclopedia of Genes and Genomes (KEGG) pathway analyses were performed on differentially expressed genes to elucidate the potential mechanism of MST1. In vitro studies were performed to investigate the effects of MST1 on SH-SY5Y model cell viability and mitochondrial function and validate the potential underlying molecular mechanisms.

**Results** MST1 overexpression accelerated neuronal degeneration and cognitive deficits in vivo while promoting oxidative stress and mitochondrial damage. Similarly, in vitro, MST1 overexpression facilitated apoptosis and mitochondrial dysfunction. MST1 knockdown and chemical inactivation reduced cognitive decline, mitochondrial dysfunction, and neuronal degeneration. Mechanistically, MST1 regulated the transcription of mitochondrial genes, including *MT-ND4L*, *MT-ATP6*, and *MT-CO2*, by binding to PGC1 $\alpha$ . Moreover, MST1 influenced cellular oxidative stress through the PI3K-Akt-ROS pathway, ultimately disrupting mitochondrial homeostasis and mediating cell damage.

**Conclusions** Cumulatively, these results suggest that MST1 primarily regulates mitochondrial DNA transcription levels by interacting with PGC1 $\alpha$  and modulates cellular oxidative stress through the PI3K-Akt-ROS pathway, disrupting mitochondrial homeostasis. This discovery can be exploited to potentially enhance mitochondrial energy metabolism pathways by targeting MST1, offering novel potential therapeutic targets for treating AD.

\*Correspondence:

Ping Wang

wping0108@163.com

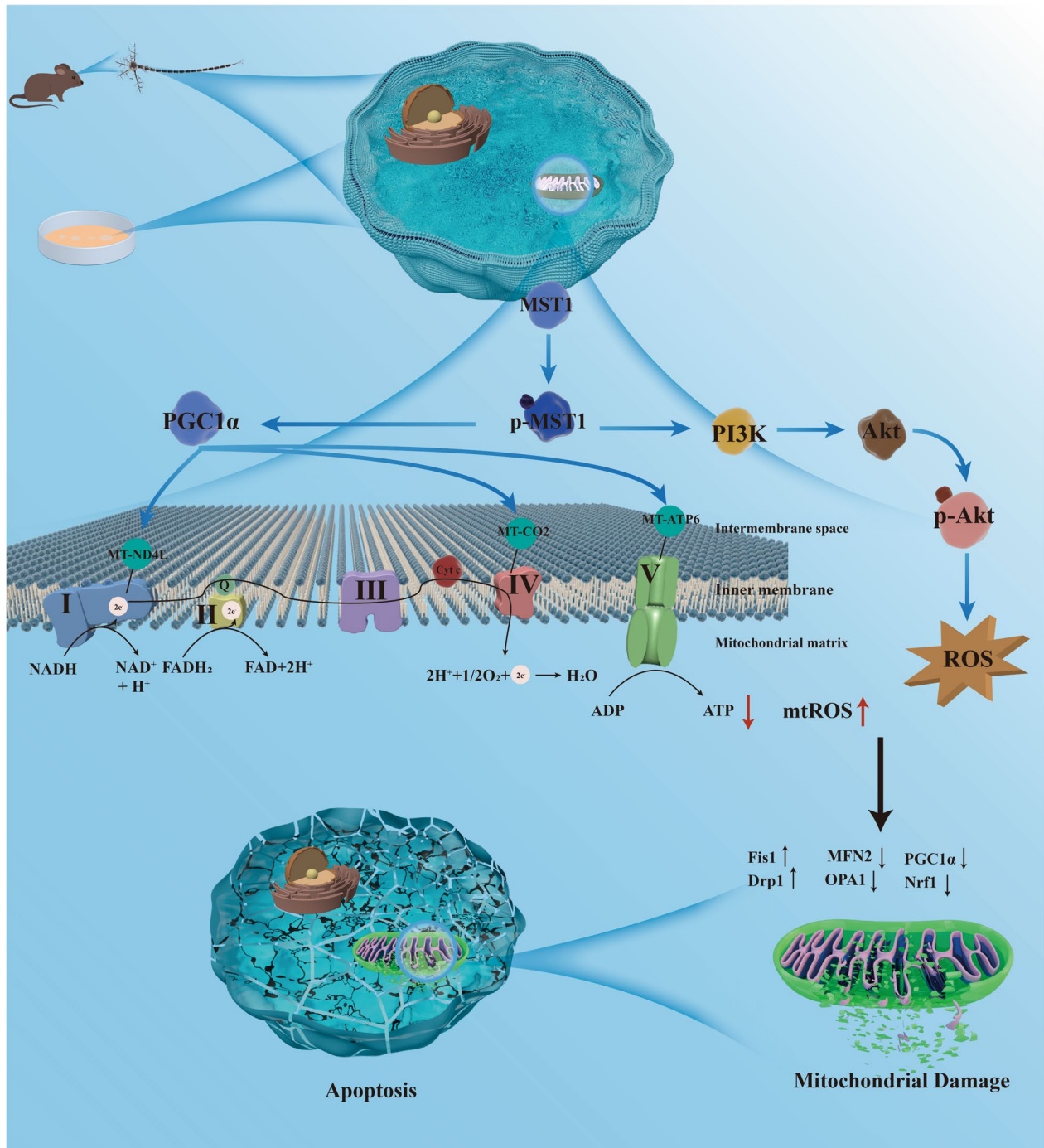
Full list of author information is available at the end of the article



© The Author(s) 2024. **Open Access** This article is licensed under a Creative Commons Attribution-NonCommercial-NoDerivatives 4.0 International License, which permits any non-commercial use, sharing, distribution and reproduction in any medium or format, as long as you give appropriate credit to the original author(s) and the source, provide a link to the Creative Commons licence, and indicate if you modified the licensed material. You do not have permission under this licence to share adapted material derived from this article or parts of it. The images or other third party material in this article are included in the article's Creative Commons licence, unless indicated otherwise in a credit line to the material. If material is not included in the article's Creative Commons licence and your intended use is not permitted by statutory regulation or exceeds the permitted use, you will need to obtain permission directly from the copyright holder. To view a copy of this licence, visit <http://creativecommons.org/licenses/by-nc-nd/4.0/>.

**Keywords** MST1, Alzheimer's disease, Mitochondrial homeostasis, Oxidative phosphorylation (OXPHOS), PI3K-Akt signaling pathway

**Graphical Abstract**



## Background

Alzheimer's disease (AD) is a predominant neurodegenerative disease and prevalent form of dementia among the elderly population. With the aging global population [1], age-related neurodegenerative ailments have emerged as a pressing public health concern. AD is characterized by the deposition of A $\beta$  plaques and the formation of tau protein neurofibrillary tangles, acknowledged as its key pathological features [2]. However, the precise pathogenesis of AD remains unclear. While certain methods exist to ameliorate symptoms, a definite cure remains elusive [3, 4]. Therefore, investigating the pathological and physiological mechanisms underlying AD is necessary to identify novel therapeutic targets.

Mitochondria—crucial organelles for energy metabolism—play a vital role in meeting the high-energy demands of neurons [5]. Additionally, mitochondria contribute over 90% of the energy required for synapses [5, 6]. Mitochondria stand as the sole organelles, apart from the nucleus, that possess their individual DNA (mtDNA) along with distinct transcription and translation mechanisms. mtDNA primarily encodes subunits that form the mitochondrial oxidative respiratory chain complex, critical for mitochondrial energy synthesis and mitochondrial homeostasis. Mitochondrial homeostasis is maintained through dynamic regulatory processes, including mitochondrial dynamics (fusion and fission), quality control (biogenesis and mitophagy) and energy metabolism (oxidative phosphorylation) [7, 8]. Recent research indicates that disruptions in mitochondrial homeostasis occur in the initial stages of AD progression [9, 10]. Dysfunction of the mitochondrial respiratory chain complex, breakdown in metabolic reprogramming, and a decreased mitochondrial content are pivotal factors contributing to the onset of AD. Moreover, mitochondrial dysfunction leads to electron leakage and decreased ATP production in the mitochondrial respiratory chain, elevating oxidative stress and neuronal damage [11, 12]. Additionally, mitochondrial oxidative stress can induce abnormal oxidative phosphorylation, triggering excessive reactive oxygen species (ROS) production within the mitochondria. This pivotal factor contributes to the dysregulation of mitochondrial homeostasis in AD [13]. Recently, targeting mitochondria and brain bioenergetics metabolism has garnered significant attention as a potentially novel therapeutic pathway toward mitigating AD progression.

Mass spectrometry and bioinformatics analyses of the brains of AD patients have revealed significant changes in the Hippo pathway. Moreover, the Hippo signaling pathway is reportedly activated in animals with AD [14–16]. Hence, manipulating this pathway may have therapeutic potential in AD prevention and treatment. The Hippo pathway represents a highly

conserved kinase-signaling pathway [17]. Mammalian Ste20-like kinase 1 (MST1)—also referred to as STK4—serves as an upstream serine/threonine kinase within the Hippo signaling pathway. In the canonical Hippo pathway, MST1 triggers the activation of downstream large tumor suppressor kinase (LATS)1/2 and YAP/TAZ kinases, regulating organ size, tissue regeneration, and tumor suppression [17, 18]. Meanwhile, in noncanonical Hippo signaling, MST1 reportedly regulates various cellular functions, including apoptosis, immune responses, and oxidative stress [19]. However, the physiological functions and intracellular signaling mechanisms of MST1 remain largely unknown. Notably, the inactivation of MST1 rescues neuronal damage in certain central nervous system diseases, including AD, Parkinson's disease, amyotrophic lateral sclerosis, intracerebral hemorrhage, and stroke-related brain injury [17]. Moreover, MST-mediated FoxO3a-Bim responds to A $\beta$ -induced neuronal death [20]. Phosphorylated MST1 also stimulates microglia activation, contributing to neuronal cell death in brain ischemic-reperfusion injury or stroke [21]. Meanwhile, more recent research has highlighted the involvement of MST1/2 in mitochondrial function. Specifically, the MST1/2-BNIP3 axis contributes to mitochondrial autophagy induction and neuronal viability regulation during mitochondrial stress [22]. MST1 is also involved in regulating mitochondrial dynamics [23–25]. However, the role of MST1 in AD progression through mitochondrial homeostasis modulation and the underlying regulatory mechanisms require experimental verification. Thus, given the multifunctionality of MST1, exploring its involvement in AD pathogenesis may identify key targets for diagnosis and treatment with significant preventive and therapeutic potential.

Considering the role of MST1 in regulating mitochondrial homeostasis in AD remains unclear, this study investigates whether MST1 influences neuronal damage and cognitive impairment in AD by regulating mitochondrial homeostasis. This study elucidates a novel role of MST1 in the onset and progression of AD, laying a theoretical foundation for identifying potential therapeutic targets.

## Methods

### Animals and drug treatment

This study sought to minimize animal usage and suffering while ensuring experiment reproducibility. The experimental mice used in this study were all male. 5xFAD and wild-type (WT) mice in the same C57BL/6 J background were purchased from Beijing Hua fu kang Biotechnology Co., Ltd. 5xFAD transgenic mice carry five FAD mutations (APP<sup>SwF1Lon</sup>, PSEN1<sup>M146L</sup>\*L286V) under the

*Thy1* promoter. All mice were housed in a specific pathogen-free facility with a 12 h light/dark cycle, temperature maintained at  $24 \pm 2$  °C, and free access to food and water.

XMU-MP-1 (HY-100526, Med Chem Express) is a reversible and selective MST1/2 inhibitor. According to the manufacturer's instructions, to prepare a 5 mg/mL stock solution, each solvent was added to the drug in the following order: 10% dimethylsulfoxide (DMSO), 40% PEG300, 5% Tween-80, and 45% saline. XMU-MP-1 was administered to the mice through intraperitoneal injection at a daily dose of 1 mg/kg for 1 month [26]. The control group mice were injected intraperitoneally with solvents without drugs.

### Cell cultures and treatment

Human neuroblastoma cells (SH-SY5Y cells) can differentiate into cells with mature neuronal morphology and biochemical properties under in vitro conditions, making them ideal for studying neuronal function and disease models. SH-SY5Y cells were procured from the Shanghai Cell Bank of the Chinese Academy of Science (Shanghai, China) and cultured in Dulbecco's modified eagle medium (DMEM, Gibco, California, USA) supplemented with 10% fetal bovine serum (FBS, Lonsera) and 1% penicillin–streptomycin (Solarbio, Beijing, China) under standard conditions of 5% CO<sub>2</sub> and 37 °C.

The  $\beta$ -amyloid (1–42) oligomer was obtained from Shanghai Qiangyao Biotechnology Co., Ltd.; 1 mg of A $\beta$ <sub>1-42</sub> oligomer powder was dissolved in 100  $\mu$ L of DMSO and subsequently mixed with 140  $\mu$ L of PBS to prepare the working solution. SH-SY5Y cells were treated with A $\beta$ <sub>1-42</sub> (20  $\mu$ M) for 24 h to establish an in vitro AD model. Cells were pre-treated with a PI3K-Akt pathway activator, 740 Y-P (25  $\mu$ M, MedChemExpress, USA), and inhibitor, LY294002 (20  $\mu$ M, MedChemExpress, USA) for 1 h [27, 28]. The drug concentrations were determined based on the drug instructions.

### Hippocampal stereotaxic injection

Adeno-associated virus (AAV)-green fluorescent protein (GFP)-MST1 and AAV-shRNA-MST1 were procured from the Shanghai GeneChem Corporation (Shanghai, China) and Hanbio Tech (Shanghai, China), respectively. The targeting sequence of AAV-shRNA-MST1 was 5'-GCCAGATTGTTGCAATCAAGC-3'. Stereotaxic injections were administered following established protocols [29]. Mice were anesthetized with pentobarbital sodium (50 mg/kg) and positioned in the stereotaxic apparatus. To ensure that AAVs were sufficiently transfected within the hippocampal region, small holes were drilled, according to the mouse brain atlas, at each injection site using the following stereotaxic coordinates: anterior–posterior position  $-2$  mm, medial–lateral

position  $\pm 1.5$  mm, 1.5 mm dorsoventral from the bregma. Subsequently, 1  $\mu$ L of AAV was injected into the bilateral hippocampus of the mice using a microinjector (0.2  $\mu$ L/min). The needle remained in place for 5 min before it was slowly withdrawn. After completing the injection, the wounds were carefully disinfected and sutured.

MST1-overexpression plasmids were procured from Jiman Biotechnology Co., Ltd. (Shanghai, China), while MST1-knockdown plasmids were obtained from Tsingke Biotechnology Co., Ltd. (Beijing, China). The targeting sequence of siRNA-MST1 was 5'-CAGAAGUGA UUCAGGAAAUTT-3'. PGC1 $\alpha$ -overexpression plasmids were purchased from Jipeng Biotechnology Co., Ltd. (Shandong, China). SH-SY5Y cells were seeded into 6-well plates at a density of  $1 \times 10^5$  cells/well and reached approximately 70–90% confluence, they were transfected with the respective plasmids using Lipofectamine<sup>TM</sup> 3000 Transfection Reagent (L3000-015, Invitrogen) according to the manufacturer's instructions.

### Morris water maze (MWM)

The Morris water maze (MWM) test comprises place navigation and spatial probe tests and assesses the spatial learning and memory abilities of mice [30]. Reference objects surrounding the pool remained consistent throughout the experiment, and the water temperature was maintained between 20 and 22 °C. During the place navigation tests, a circular opaque platform was positioned 1 cm below the water surface at the center of the target quadrant. Mice were gently placed into the water, facing the wall, from four random quadrants for 5 days. They were given 60 s to locate the hidden platform. Time and swimming trajectories were recorded using an automatic camera system. If the mice failed to reach the hidden platform within 60 s, they were guided to it and allowed to remain there for 20 s. On the final day, the platform was removed for the spatial probe experiment. The number of crossings over the original hidden platform and time spent swimming in the target quadrant within 60 s were recorded.

### Transmission electron microscopy (TEM)

The fresh mouse hippocampal tissue was cut into small pieces (1 mm  $\times$  1 mm  $\times$  3 mm) and promptly immersed in a 3% glutaraldehyde fixing solution. The TEM samples were prepared using a conventional method. All samples were rinsed, fixed with 1% osmium tetroxide, dehydrated, embedded in Epon, and sectioned into ultrathin slices (70–100 nm). Subsequently, they were stained with lead citrate and uranium acetate. Finally, the ultrastructure and morphology of the mitochondria were visualized using a transmission electron microscope (JEOL-1200E).

### Immunofluorescence (IF)

After behavioral testing, mice underwent cardiac perfusion with precooled 4% paraformaldehyde (PFA). Subsequently, the brains were removed and immersed in 4% PFA at 4 °C for 24 h. Brain tissue samples were dehydrated using a sucrose gradient and embedded in an optimal cutting temperature (OCT) compound (SAKURA, Japan). The brain tissues were sectioned into 20 µm slices using a freezing microtome (Leica, USA). Brain slices were fixed in 4% PFA for 20 min, washed with PBS thrice, and subjected to antigen retrieval with an antigen repair solution for 5 min at room temperature (20–25 °C). Following incubation with 1% TritonX-100 and 5% goat serum, brain slices were incubated with primary antibodies overnight at 4 °C. This included an anti-p-MST1 antibody (1:100, Bioss), anti-PSD95 antibody (1:200, Abclonal), and anti-SYP antibody (1:200, Abcam). Subsequently, slices were incubated with a secondary antibody (goat antirabbit IgG Alexa Fluor Plus 488, 1:500, Abcam) for 1 h at room temperature (20–25 °C). DAPI-containing anti-fluorescence quencher (Sigma) was utilized for nuclear staining. Images were captured with a laser scanning confocal microscope (Zeiss, LSM 800, Germany) and a multispectral imaging system (PerkinElmer, Mantra, America) and further analyzed using ImageJ.

### Thioflavin-S staining

To observe amyloid plaque deposition, thioflavin-S staining was performed. The 30 µm brain slices were rinsed with PBS thrice and mounted onto glass slides. According to the manufacturer's instructions, brain sections were stained with 1% thioflavin solution (Solarbio) at room temperature (20–25 °C) for 5 min. The slices were then rinsed with 50% alcohol twice for 5 min each. Images were captured using a multispectral imaging system (PerkinElmer, MA, USA). Image analysis was performed by researchers blinded to the treatment groups using ImageJ software.

### Immunohistochemistry (IHC)

Immunohistochemical techniques were employed to assess the expression level of p-MST1 protein. Brain tissues were embedded in paraffin and sectioned into 5 µm slices. The sections underwent dewaxing, rehydration, antigen repair using EDTA antigen repair solution (G1203, Servicebio, Wuhan), and inactivation of endogenous peroxidase with 3% hydrogen peroxide solution. Sections were incubated with 3% bovine serum albumin (BSA) at room temperature (20–25 °C) for 30 min and incubated overnight at 4 °C with an anti-p-MST1 antibody (4635R, Bioss, 1:100). Subsequently, sections were incubated with HRP-labeled goat antirabbit IgG (GB23303, Servicebio, 1:200) at room temperature

(20–25 °C) for 50 min. Sections were stained with diaminobenzidine (DAB) and hematoxylin for 3 min. Images were visualized with a digital pathology scanner (NanoZoomer S60, Japan).

### Hematoxylin/eosin staining (HE)

After dewaxing and rehydration, the 5-µm paraffin sections underwent treatment with hematoxylin–eosin (HE) constant staining pretreatment solution for 1 min. They were then immersed in hematoxylin solution for 3–5 min. Subsequently, the sections were sequentially treated with hematoxylin differentiation solution and hematoxylin blue solution. The samples were rinsed with tap water after each dyeing step. The sections were immersed in 95% ethanol for 1 min and in eosin dye for 15 s. They were then dehydrated in absolute alcohol, rendered transparent using xylene, and sealed with neutral gum. Images were captured using a digital pathology scanner (Nano Zoomer S60, Japan).

### Nissl staining

Histologically, neuronal morphological changes were assessed using Nissl staining. Dewaxed and hydrated 5 µm tissue sections were treated with Nissl's stain for 2–5 min, followed by immersion in 1% glacial acetic acid. The reaction was terminated by washing with running water. Subsequently, the slices were rendered transparent with xylene for 10 min and sealed with gum. Images were captured using a digital pathology scanner (Nano Zoomer S60, Japan).

The differentiation of live and dead cells was based primarily on their morphological characteristics; only neurons with rounded morphology and visible nuclei were considered live cells. Dead cells exhibit disrupted cell membranes, alterations in cell size and shape, chromatin condensation, and nuclear condensation due to cellular damage [31]. Morphological changes in the hippocampal neurons (DG, CA1, and CA3 regions) were assessed in mice, utilizing the ImageJ software. Live and dead cells were counted separately.

### Western blotting

Total protein samples were extracted from the cultured SH-SY5Y cells or hippocampal tissues subjected to various treatments using cool radio immunoprecipitation assay (RIPA) lysis buffer (Beyotime, Shanghai, China). Protein quantification was performed using a BCA kit (Solarbio). Protein samples were heated with 5×loading buffer (Beyotime) at 95 °C for 10 min. The protein samples (30–60 µg) and protein ladder (26616, Thermo Fisher Scientific, USA) were loaded and electrophoresed on SDS-PAGE gel (10%, 12.5%, 15%). Proteins were transferred to polyvinylidene fluoride (PVDF) membranes

(Merck Millipore, Darmstadt, Germany) for 1–2 h and blocked with 5% nonfat milk solution for 1.5 h. The membranes were incubated with primary antibodies overnight at 4 °C and then immersed in a secondary antibody solution for 1 h. Finally, protein expression was detected using enhanced chemiluminescence (ECL) western blotting (WB) detection reagents (Merck Millipore), and images were captured by a chemiluminescence imager (Tanon4800, Shanghai, China). Table S1 presents the details for all antibodies used.

#### Co-immunoprecipitation (Co-IP)

SH-SY5Y cells were transfected with a FLAG-tagged MST1 plasmid and resuspended in cell lysis buffer for WB and IP (Beyotime, Shanghai, China) supplemented with 1% protease inhibitors (Beyotime) and 1% phosphatase inhibitors (Beyotime). The samples were centrifuged at  $13,000 \times g$  for 10 min at 4 °C, and the supernatant containing protein was collected. Subsequently, the total protein concentration was determined using a BCA assay kit. One hundred microliters of the samples were allocated for use as the input group. The remaining samples were mixed with flag magnetic beads (HY-K0207, MedChemExpress, USA) and incubated overnight at 4 °C on a rotary mixer. The following day, the magnetic beads were retrieved using a magnetic rack and washed with TBST. Subsequently, the input group sample and magnetic beads were mixed in a loading buffer and heated at 95 °C for 10 min. Potential interactors of MST1 were detected using SDS-PAGE.

#### Real-time quantitative polymerase chain reaction (RT-qPCR)

Total RNA from the cells and brain tissues was isolated using the RNA-Quick Purification Kit (ES Science Biotech, Shanghai) following the manufacturer's instructions. Using the Evo M-MLV RT Kit (from Accurate Biotechnology Co., Ltd.), synthesize cDNA from one microgram of RNA under reaction conditions of 42 °C for 2 min. Using SYBR qPCR Master Mix (Vazyme, Nanjing, China) and specific primers, the mRNA levels of genes were quantitatively determined through the QuantStudio™5 Real-Time PCR System (ThermoFisher Scientific, USA) under specific reaction conditions. The relative gene expression levels were calculated using the classical  $2^{(-\Delta\Delta Ct)}$  method.

#### RNA-seq

Total RNA was extracted from the hippocampal tissue of mice using TRIzol™ reagent (Novogene) and utilized as input material for RNA library preparation. To ensure library quality, RT-qPCR was conducted to

accurately quantify the effective concentration of the library ( $>1.5$  nM). Different libraries were sequenced by Novogene using an Illumina NovaSeq 6000 Sequencing System. For differential gene analysis, padj (FDR-adjusted p-values)  $\leq 0.05$  and  $\log_2$  (foldchange)  $\geq 1.0$  were set as the thresholds for significant differential expression.

#### Enzyme-linked immunosorbent assay (ELISA)

The  $A\beta_{1-42}$  level in mouse hippocampal tissue was assessed using an ELISA kit (Elabscience Biotechnology Co., Ltd.). The hippocampal tissue was weighed, cut into small pieces, and homogenized with PBS at a 1:9 ratio. The homogenate was centrifuged at 5000 g for 10 min, and the supernatant was collected. Per the manufacturer's instructions, 100  $\mu$ L of standard/sample was added to each well and incubated at 37 °C for 1.5 h. Next, 100  $\mu$ L of the biotin-labeled antibody working solution was added and incubated at 37 °C for 1 h. The plates were then washed with wash buffer and 100  $\mu$ L of the HRP enzyme conjugate working solution was added to each well and incubated for 30 min at 37 °C. Next, plates were washed again and 3,3',5,5'-tetramethylbenzidine (TMB) substrate was added to each well and incubated in the dark at 37 °C for 15 min. Finally, stop solution was added and the optical density (OD) value was immediately measured at 450 nm with a microplate reader (Biotek, Vermont, USA).

#### Cell-counting-kit 8 (CCK-8) assay

SH-SY5Y cells were seeded in 96-well plates at a density of 8000 cells/well. Following incubation, CCK8 reagent (MedChemExpress) was added to the medium at a 1:100 ratio and incubated for 2–4 h to assess cell viability. The optical density (OD) value at 450 nm was measured using a microplate reader (Biotek, Winooski, Vermont, USA).

#### Flow cytometry

SH-SY5Y cells were seeded into 6-well plates. Following transfection, modeling, and treatment with drugs, the cells were incubated in a 10  $\mu$ M DCFH-DA solution (Elabscience Biotechnology Co., Ltd.) for 60 min at 37 °C in the dark. Subsequently, the cells were collected and resuspended in a serum-free medium. The intensity of green fluorescence, indicative of intracellular ROS levels, was measured by flow cytometry (Beckman coulter, USA).

An Annexin V-FITC/PI apoptosis detection kit (Vazyme) was utilized to assess cell apoptosis levels. Cells were harvested and washed twice with precooled PBS. Subsequently, they were gently resuspended in  $1 \times$  Annexin V-FITC/PI binding buffer and incubated with annexin-V-FITC and PI at room temperature (20–25 °C) for 10 min in the dark. Apoptotic cells were detected by flow cytometry (Beckman). Based on the

bicolor flow cytometry scatter plot, cells that were double-negative for Annexin V-FITC and PI were considered normal cells; cells that were Annexin V-FITC-positive and PI-negative were considered early apoptotic cells; cells that were double-positive for Annexin V-FITC and PI were considered late apoptotic cells. Using this classification, the proportion of apoptotic cells was calculated. All data were analyzed using FlowJo v10 (FlowJo LLC) software.

#### **Oxidative stress assay**

Mouse hippocampal tissue was homogenized in normal saline (mass ratio of 1:9) using a tissue homogenizer. The homogenate was centrifuged at 12,000 g for 10 min at 4 °C, and the supernatant was collected. The levels of oxidative stress indicators (total superoxide dismutase (T-SOD), glutathione peroxidase (GSH-PX), and malondialdehyde (MDA)) were measured with commercial reagent kits (Nanjing Jian Cheng Bioengineering Institute) according to the manufacturers' instructions.

#### **Probes for mitochondrial detection**

SH-SY5Y cells were cultured in confocal dishes and treated according to experimental requirements. To assess mitochondrial membrane potential (MMP), tetramethylrhodamine methyl ester (TMRM) staining solution (Invitrogen, USA) was introduced to the cell growth medium at a final concentration of 50 nM and incubated for 20 min at 37 °C. To assess mitochondrial oxidative stress, MitoSOX™ Red reagent (Invitrogen)—a mitochondrial superoxide indicator—was added to cells at a final concentration of 5 μM and incubated for 20 min at 37 °C in the dark. To evaluate mitochondrial morphology, the MitoTracker probe (Invitrogen) was introduced to the cell medium at a final concentration of 100 nM and incubated for 30 min at 37 °C in the dark. Hoechst 33342 nuclear staining dye and DAPI were utilized for nuclei staining. The fluorescence intensity of the cells was observed using laser scanning confocal microscope (LSM 800, Zeiss, Germany).

#### **ATP level measurement**

ATP levels in cells or tissues were assessed using an Enhanced ATP Assay Kit (S0027, Biotechnology, Shanghai, China), following the instructions of the manufacturer. Cell or tissue samples were lysed in ATP detection lysate and centrifuged at 12,000 g for 5 min at 4 °C to obtain the supernatant. The cell or tissue supernatants were promptly added to the ATP detection working solution. The relative light unit (RLU) value of the sample was immediately measured using a cell Imaging Multi-Mode reader (Biotec, Cytation5, USA).

#### **Measurement of mitochondrial respiratory capacity**

The oxygen consumption rate (OCR) representing the mitochondrial respiratory capacity of SH-SY5Y cells was assessed using the XF Cell Mito Stress Test Kit (Agilent, USA, California) on a Seahorse XFe24 Analyzer (Seahorse Bioscience/Agilent Technologies, North Billerica, MA), following a standard protocol. SH-SY5Y cells were seeded in Seahorse XFe24 plates (80,000 cells/well). The mitochondrial stress test experiment measured the OCR of SH-SY5Y cells by sequentially introducing targeted drugs to the mitochondrial electron transport chain (ETC), including 1.5 μM oligomycin (ATP synthase inhibitor), 2 μM phenylhydrazine (FCCP; mitochondrial respiration uncoupler), and 0.5 μM rotenone/antimycin A (complete respiratory inhibitor). Key parameters reflecting mitochondrial function were obtained, including basal respiration, ATP-linked respiration, proton leak, and maximum respiration. Subsequently, cells were lysed in 1×RIPA buffer and total protein quantification was conducted on each well sample. The data were then normalized.

#### **Mitochondria isolation and complex activity**

Mitochondria were isolated from cells using a cell mitochondria separation and extraction kit (KTP4003, Abbkine, Wuhan, China). Initially, cells were harvested and washed by suspending the cell pellet in ice-cold PBS, followed by centrifugation at 500×g for 3 min, after which the PBS was discarded. The cell pellets were resuspended in cold lysis buffers A, B, and C, and the mixture was centrifuged at 600×g for 10 min. Finally, the supernatant was collected and centrifuged at 11,000×g for 10 min at 4 °C. The resulting sediment contained the isolated mitochondria. According to the manufacturer's instructions, the activity of mitochondrial complexes I–V was measured using the mitochondrial respiratory chain complex activity detection kit (Abbkine, Wuhan, China).

#### **Statistical analysis**

Statistical analyses were conducted using GraphPad Prism 8.0 software, and results were presented as mean ± standard error of the mean (SEM). Statistical differences between two groups were assessed using an unpaired two-tailed Student's *t*-test. One-way analysis of variance (ANOVA) was used to compare multiple exposure groups, followed by Tukey's multiple comparison test. Data from the MWM test was analyzed using two-way ANOVA with the Bonferroni multiple comparison test. RNA-seq data were analyzed by R (4.1.1). All experiments were repeated at least three times. Statistical significance was defined at  $p < 0.05$ .

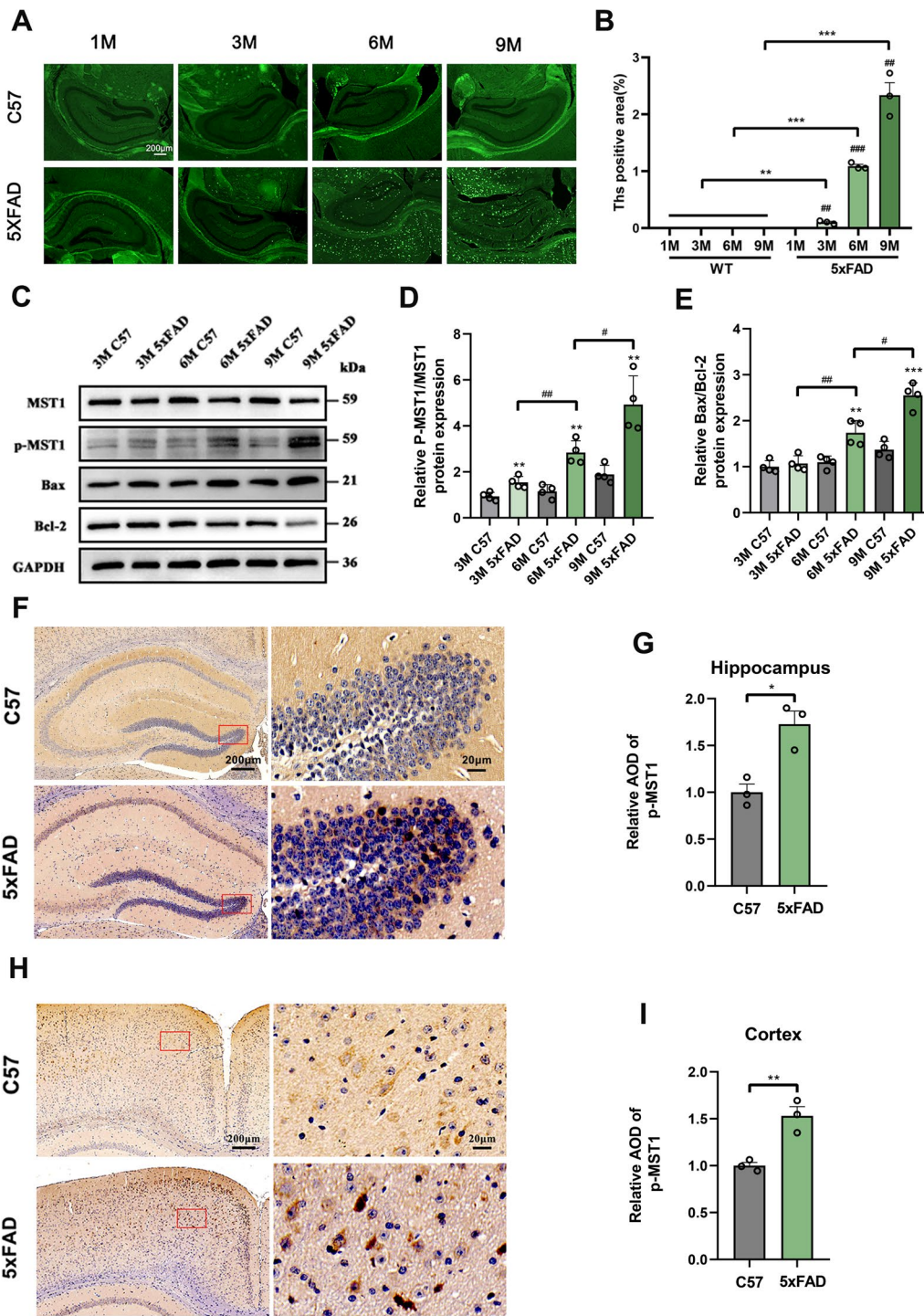


**Fig. 1** Activation of MST1 is involved in the pathological process of 5xFAD mice. **A** Representative thioflavin S staining images for detection content in the hippocampus of 1-, 3-, 6-, 9-month-old WT and 5xFAD mice. **B** Quantitative analysis of the fluorescence intensity of amyloid plaque in the hippocampus of 1-, 3-, 6-, 9-month-old WT and 5xFAD mice (n=3). **C** Hippocampus MST1, p-MST1, Bax, and Bcl-2 protein levels in 3-, 6-, 9-month-old WT and 5xFAD mice as showed using immunoblotting analysis. **D** Quantitative analysis of p-MST1/MST1 (n=4). **E** Quantitative analysis of Bax/Bcl-2 (n=4). **F–I** Representative immunohistochemical images and relative expression of p-MST1 in the hippocampus (**F, G**) and cortex (**H, I**) of 6-month-old WT and 5xFAD mice (n=3, Scale bar is 200 μm and enlarged images scale bar is 20 μm). Nuclei were stained in blue (DAPI). All data represent means ± SEMs. \*, 5xFAD vs. WT group at different months of age. \*p < 0.05; \*\*p < 0.01 and \*\*\*p < 0.001. #, Comparison between 5xFAD at different months of age, #p < 0.05; ##p < 0.01



## Results

### MST1 activation is associated with disease progression in 5xFAD mice

Labeling amyloid content and distribution in the brain parenchyma is a crucial indicator for evaluating the pathological status of AD. In 5xFAD mice, the presence of A $\beta$ <sub>1-42</sub> emerges at an early age and progressively increases thereafter, facilitating the early formation of amyloid deposition plaques [32]. Therefore, amyloid plaque deposition was assessed in the brains of 5xFAD mice at 1, 3, 6, and 9 months old using thioflavin staining. Mature amyloid plaques were present in the hippocampus and cortex beginning at 3 months, with deposition gradually intensifying as the mice aged (Fig. 1A, B).

To explore the activation of MST1 in 5xFAD, its activated form p-MST1 (Thr183) was assessed. The WB results showed a gradual increase in the p-MST1 to MST1 ratio as the age of 5xFAD mice increased, aligning with the observed changes in hippocampal neuronal apoptotic protein Bax and amyloid plaque deposition. However, these results did not differ significantly in age-matched WT mice. Therefore, the activation of MST1 to p-MST1 in 5xFAD mice may correlate with the pathological advancement of the disease (Fig. 1C–E). To further validate p-MST1 activity and distribution, IHC assays were conducted, revealing a significant increase in p-MST1 levels within the hippocampus (Fig. 1F, G) and cortex (Fig. 1H, I) of 6-month-old 5xFAD mice compared with the WT group, consistent with the WB results.

### MST1 promotes cognitive deficits and neuronal damage in 5-month-old 5xFAD mice

To assess the effect of MST1 on cognitive and memory impairment in AD mice, 4-month-old C57 mice and 5xFAD mice were randomly assigned to four groups: C57 + AAV vehicle, C57 + AAV MST1, 5xFAD + AAV vehicle, and 5xFAD + AAV MST1, with 20 animals in each group. AAV-GFP vehicle and the AAV-GFP MST1 were administered into the DG region of mice through hippocampal stereotaxic injection to upregulate MST1 (Fig. 2A). Four weeks post-injection, spontaneous GFP

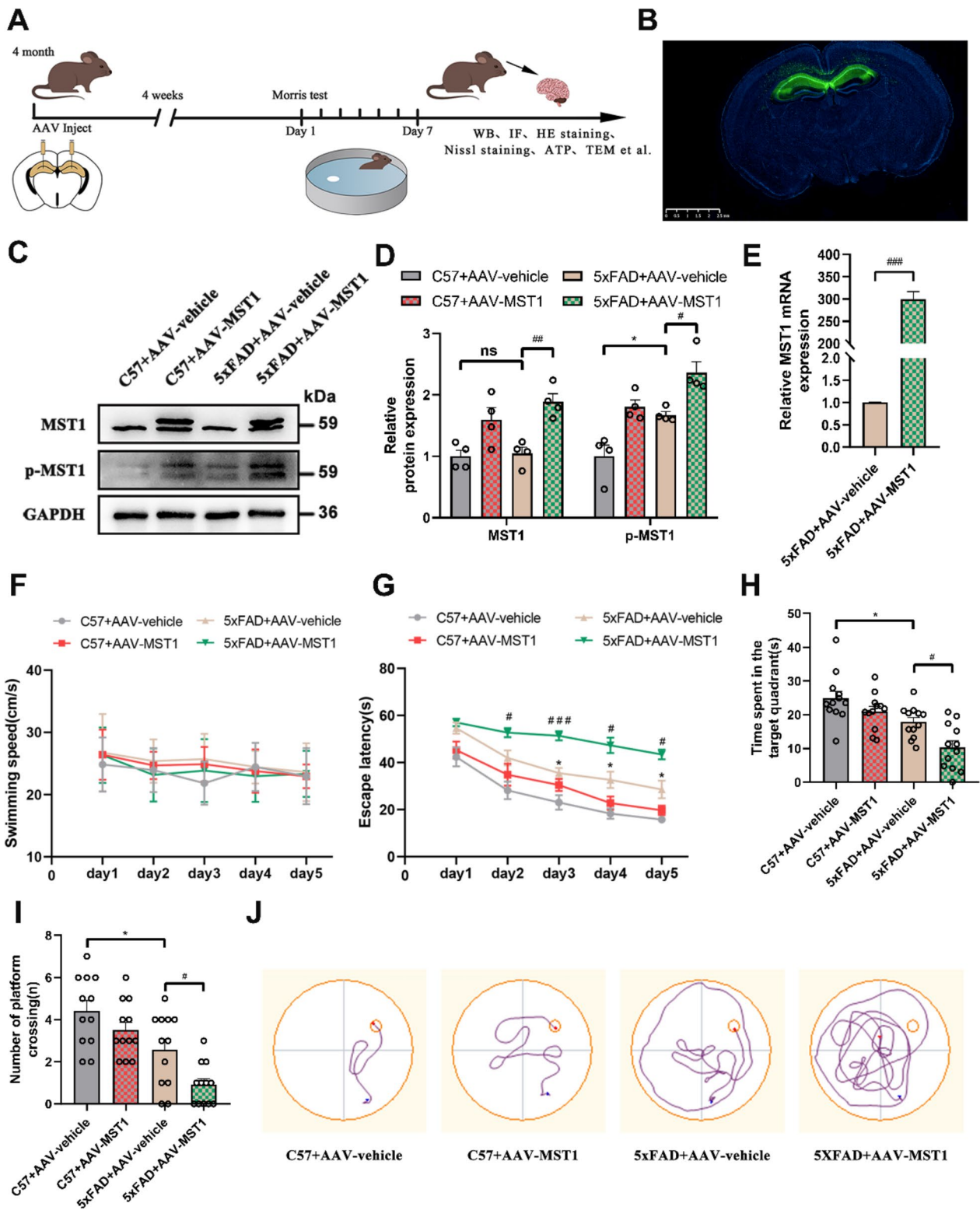
fluorescence from the virus was observed in the hippocampus, indicating successful injection (Fig. 2B). The expression efficiency of MST1 was also evaluated via WB and RT-qPCR. The results showed significantly higher levels of MST1 expression at the protein and mRNA levels than in the control group (Fig. 2C–E).

Four weeks post-injection, the MWM test was performed to assess the spatial learning and memory abilities of the mice. During the training period, the mice did not exhibit significant differences in swimming speed (Fig. 2F). Compared with the C57 + AAV-vehicle group, the 5xFAD + AAV-vehicle group exhibited a significantly prolonged escape latency (time to find the hidden platform) beginning from the third day of training. Moreover, the escape latency of the 5xFAD + AAV-MST1 group during the training was significantly longer than that of the 5xFAD + AAV-vehicle group (Fig. 2G, J). The number of platform crossings and total time spent in the target quadrant were reduced considerably in the 5xFAD + AAV-MST1 group compared with the 5xFAD + AAV-vehicle group. Similar reductions were observed in the 5xFAD + AAV-vehicle group compared with the C57 + AAV-vehicle group (Fig. 2H, I). These MWM results suggested that MST1 overexpression exacerbated spatial learning and memory impairment in 5xFAD mice.

Due to the pivotal role of neuronal loss in cognitive decline, we examined the effect of MST1 expression on neurons in the CA1, CA3, and DG regions of the hippocampus using Nissl and HE staining, and then assessed the cellular morphology changes and the level of cellular death. Nissl staining showed neurons have normal morphology, clear nuclei, and dense arrangement in the C57 + AAV-vehicle group. However, hippocampal neurons in the 5xFAD + AAV vehicle group were mostly damaged (vacuolated, shrunk, and loosely arranged), having a dramatic reduction in the live: dead neuronal ratio. Furthermore, the degree of neuronal damage in the 5xFAD + AAV-MST1 group was more severe, and the live: dead neuronal ratio was further

(See figure on next page.)

**Fig. 2** MST1 Overexpression aggravates cognitive impairment in 5-month 5xFAD mice. **A** Schematic diagram of experimental arrangement. AAV-GFP-vehicle and AAV-GFP-MST1 was injected into the hippocampus of 4-month C57 mice and 5xFAD mice, and then the mice were divided into four groups: C57 + AAV vehicle, C57 + AAV MST1, 5xFAD + AAV vehicle, and 5xFAD + AAV MST1 for experiments. One month later, MWM test was performed, and finally all mice were euthanized for other experiments. **B** Representative spontaneous fluorescence images of the AAVs-infected slices (n=4, Scale bar is 2.5  $\mu$ m). **C** Representative immunoblotting bands of hippocampus MST1 and p-MST1 after AAVs injection. **D** Quantitative analysis of MST1 and p-MST1 in hippocampus (n=4). **E** MST1 mRNA levels in the hippocampus after AAVs injection were detected using RT-qPCR (n=3). **F–J** MWM test results of four groups of mice, including swimming speed (**F**), escape latency (**G**), total time spent in the target quadrant (**H**), number of platform crossings (**I**), representative traces on fifth day the MWM training period (**J**). (n = 12). All data represent means  $\pm$  SEMs. \*, Comparison between C57 + AAV-vehicle and 5xFAD + AAV-vehicle group, \**p* < 0.05; #, Comparison between 5xFAD + AAV-vehicle and 5xFAD + AAV-MST1 group, #*p* < 0.05; ##*p* < 0.01; ###*p* < 0.001



reduced compared to the 5xFAD + AAV vehicle group (Fig. 3A, B).

HE staining revealed a compact arrangement and normal morphology of neuronal cells in the C57 + AAV vehicle group. In contrast, the 5xFAD + AAV vehicle group exhibited sparse neuron arrangement with some pyknotic nuclei and increased chromatin. MST1 overexpression further aggravated the increase in the number of abnormal neurons (Fig. 3C).

Additionally, the expression of apoptosis-related proteins (Bax, Bcl-2, Cleaved Caspase 9, Cleaved Caspase 3, and Cyt-C) was assessed through immunoblotting. The Bax/Bcl-2 ratio and expressions of Cleaved Caspase 9, Cleaved Caspase 3, and Cyt-C in the 5xFAD + AAV vehicle group were significantly higher than in the C57 + AAV vehicle group. In the 5xFAD + AAV-MST1 group, the expression levels of apoptosis-related proteins were higher than in the 5xFAD + AAV vehicle group (Fig. 3D, E). These data suggest that MST1 promoted neuronal apoptosis.

Finally, WB revealed reduced expression levels of the synaptic marker proteins PSD95 and SYP in the 5xFAD + AAV-MST1 group compared with the 5xFAD group (Fig. S1A, B). IF of PSD95 and SYP validation yielded similar results (Fig. 3F–H), suggesting that MST1 overexpression also impaired the synaptic structure of neurons. ELISA results further revealed that A $\beta$  deposition did not differ significantly between the 5xFAD + ad-MST1 and 5xFAD + ad-vehicle groups, implying that overexpression of MST1 did not significantly increase A $\beta$ <sub>1-42</sub> content (Fig. 3I).

Collectively, these findings suggest that MST1 promotes neuronal apoptosis and exacerbates the pathological process in 5xFAD mice through a mechanism that does not involve increased A $\beta$  deposition.

### MST1 exacerbates mitochondrial dysfunction and oxidative stress levels in 5-month-old 5xFAD mice

Mitochondria play an important role in satisfying the high energy metabolism of neurons, contributing more than 90% of the energy required by synapses. Hence,

mitochondrial dysfunction causes significant damage to neurons. Mitochondrial dysfunction can manifest as changes in mitochondrial ultrastructure, increased mitochondrial fission, decreased fusion and biogenesis, increased ROS, and reduced ATP production. The mitochondrial perimeter is indicative of morphological alterations [33]. Hence, TEM was employed to monitor mitochondrial ultrastructural changes in mouse hippocampal neurons. The mitochondrial morphology (round or oval) appeared normal, exhibiting clear and intact outer membranes and cristae in the C57 + AAV vehicle group. Moreover, the mitochondrial perimeter was relatively longer in the C57 + AAV vehicle group. Although the mitochondria exhibited abnormal morphology and smaller perimeters in the C57 + AAV-MST1 group, there was no statistically significant difference when compared to the C57 + AAV vehicle group (Fig. 4A, B). However, in the 5xFAD + AAV-vehicle and 5xFAD + AAV-MST1 groups, some of the mitochondria exhibited significant shrinkage, swelling, and incomplete cristae, accompanied by decreased matrix density and shortened perimeters. The mitochondrial morphology in the 5xFAD + AAV-MST1 group deteriorated further than in the 5xFAD + AAV-vehicle group (Fig. 4A, B). This suggests that MST1 overexpression in 5xFAD mice exacerbates mitochondrial morphological and ultrastructural damage.

The WB results showed significant variations in mitochondrial dynamic-related proteins (OPA1, MFN2, Drp1, and Fis1) and mitochondrial biogenic proteins (PGC1 $\alpha$  and Nrf1) between the C57 + AAV-vehicle and 5xFAD + AAV-vehicle groups, as well as between the 5xFAD + AAV-vehicle and 5xFAD + AAV-MST1 groups (Fig. 4C, D). Hence, compared with the C57 + AAV-vehicle group, the mitochondrial fission in the 5xFAD group increased, while the mitochondrial fusion and biogenesis decreased. Notably, MST1 overexpression in 5xFAD mice further increased mitochondrial fission and inhibited mitochondrial fusion and biosynthesis compared with the 5xFAD + AAV-vehicle group.

(See figure on next page.)

**Fig. 3** MST1 Overexpression aggravates neuronal damage in 5-month 5xFAD mice. **A** Representative Nissl staining images of hippocampal three subregions (DG, CA1 and CA3) in different group (Scale bar is 200  $\mu$ m and enlarged images scale bar is 50  $\mu$ m). red arrows indicate dead neuronal cells. **B** The ratio of live and dead neuronal cells of the hippocampus in different groups (n=4). **C** HE staining images of hippocampal three subregions (DG, CA1 and CA3) in different group (n=3, Scale bar is 200  $\mu$ m and enlarged images scale bar is 50  $\mu$ m). **D** Representative immunoblotting bands of hippocampus Bax, Bcl-2, Cleaved Caspase 9, Cleaved Caspase 3, and Cyt-C after AAVs injection **E** Quantitative analysis of Bax/Bcl-2, Cleaved Caspase 9, Cleaved Caspase 3, and Cyt-C in hippocampus (n=4). **F–H** Representative immunofluorescence images and quantitative analysis of PSD95 and SYP in the hippocampus DG region of different group (n=4, Scale bar is 50  $\mu$ m). Nuclei were stained in blue (DAPI). **I** The levels of A $\beta$ <sub>1-42</sub> in the hippocampus of different group were measured using ELISA (n=4). All data represent means  $\pm$  SEMs. \*, Comparison between C57 + AAV-vehicle and 5xFAD + AAV-vehicle group, \* $p$  < 0.05; \*\* $p$  < 0.01; \*\*\* $p$  < 0.001; #, Comparison between 5xFAD + AAV-vehicle and 5xFAD + AAV-MST1 group, # $p$  < 0.05; ## $p$  < 0.01. ns, no significance

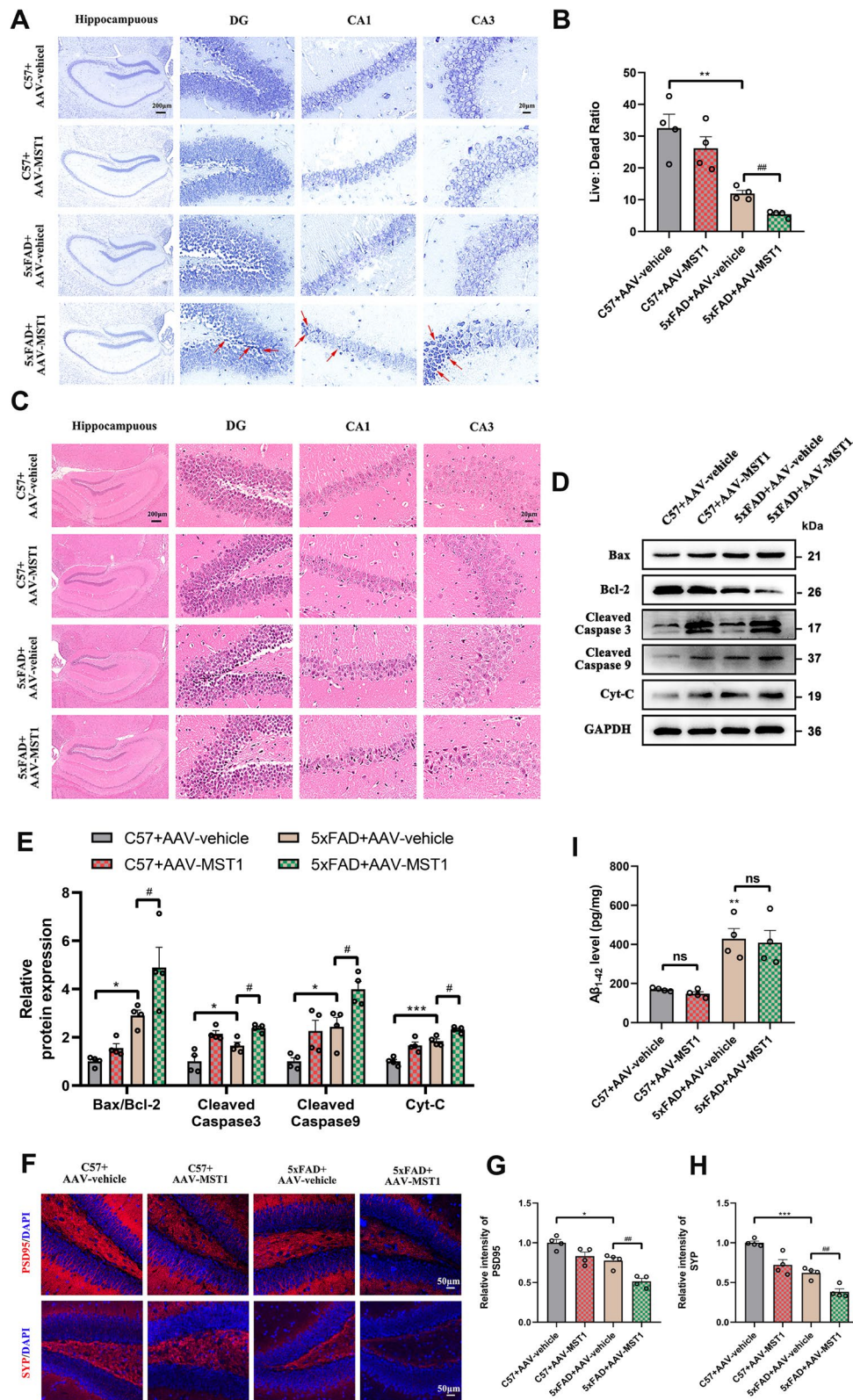


**Fig. 3** (See legend on previous page.)

The impact of MST1 overexpression on 5xFAD mice mitochondrial oxidative stress was also evaluated via MitoSOX red fluorescence staining. Mitochondrial ROS in the C57 + AAV-MST1 group increased, with no significant differences compared with the C57 + AAV-vehicle group. In contrast, the MitoSOX red fluorescence staining in the 5xFAD + AAV-vehicle group tended to increase compared to the C57 + AAV-vehicle group. Meanwhile, significantly more mitochondrial ROS was detected in the 5xFAD + AAV-MST1 group compared with the 5xFAD + AAV-vehicle group (Fig. 4E, F and Fig. S1C, D). These results confirmed that MST1 could enhance the mitochondrial ROS level in the hippocampus of 5xFAD mice, further aggravating mitochondrial damage.

ATP levels were reduced in the 5xFAD + AAV-vehicle group compared with the C57 + AAV-vehicle group. Importantly, the reduction in ATP levels was more pronounced in 5xFAD mice overexpressing MST1 (Fig. 4G). These data suggest that overexpression of MST1 interferes with energy metabolic processes in 5xFAD mice.

The activities of SOD, GSH, and MDA serve as indicators of cellular oxidative stress levels. In the 5xFAD + AAV-vehicle group, the levels of SOD and GSH decreased (Fig. 4H, I), while MDA increased (Fig. 4J) compared with the control group. Meanwhile, the 5xFAD + AAV-MST1 group exhibited significantly reduced SOD and GSH levels, along with a significant increase in MDA activity compared with the 5xFAD + AAV-vehicle group (Fig. 4H–J). Hence, MST1 promoted oxidative stress in 5xFAD mice.

Taken together, these findings imply that overexpression of MST1 in the hippocampus of 5xFAD mice impairs mitochondrial morphology and function, causing oxidative stress and imbalanced energy metabolism, which leads to hippocampal damage and exacerbation of cognitive deficits in mice.

#### Down-regulation of MST1 alleviates cognitive impairment and mitochondrial dysfunction in 8-month-old mice

To verify the effect of MST1 downregulation on cognition, mitochondrial function, and neurons in AD mice, AAVs were administered into the DG region of

7-month-old C57 and 5xFAD mice (Fig. 5A). Four weeks later, a significant decrease in MST1 protein and mRNA expression levels was observed compared with the control group (Fig. 5B–D). Additionally, the abundance of p-MST1 protein was significantly lower than in the control group (Fig. 5B, C).

Subsequently, the MWM was employed to assess the spatial learning and memory of each mouse group. The mice did not exhibit significant differences in swimming speed during the training period (Fig. 5E). The 5xFAD + AAV-vehicle group exhibited a significantly prolonged escape latency (time to find the hidden platform) starting from the third day of training compared with the C57 + AAV-vehicle group. Meanwhile, the escape latency was significantly shorter in the 5xFAD + AAV-shMST1 group during the training compared to the 5xFAD + AAV-vehicle group (Fig. 5F, I). The number of platform crossings and total time spent in the target quadrant were reduced considerably in the 5xFAD + AAV-vehicle compared with the C57 + AAV-vehicle group. These factors were significantly increased in the 5xFAD + AAV-shMST1 mice compared with the 5xFAD + AAV-vehicle group (Fig. 5G, H). These MWM results showed that MST1 knockdown improved the ability to locate the hidden platforms and enhanced the cognitive function of 8-month-old 5xFAD mice.

To observe the effect of knocking down MST1 on neuronal synapses, immunofluorescence staining of synaptic-related markers (PSD95 and SYP) in the DG region of the hippocampus was performed. A significant reduction in synapse-related proteins was observed in 8-month-old 5xFAD mice, whereas MST1 knockdown significantly increased the abundance of these proteins in 5xFAD mice (Fig. S2A–C). These results indicate that 8-month-old 5xFAD mice experience significant synaptic damage, which can be prevented by MST1 knockdown.

Compared with the 5xFAD + AAV-vehicle group, The 5xFAD + AAV-shMST1 mice exhibited significantly increased abundances of mitochondrial fusion (OPA1 and MFN2) and biogenic (PGC1 $\alpha$  and Nrf1) proteins and a significant decrease in mitochondrial fission proteins (Drp1 and Fis1) (Fig. 5J, K). MitoSOX red staining results

(See figure on next page.)

**Fig. 4** MST1 Overexpression aggravates mitochondrial damage and oxidative stress levels in 5-month 5xFAD mice. **A** Morphological change of mitochondria in hippocampal neurons was measured by transmission electron microscopy after AAVs injection (Scale bar is 500 nm). red arrows indicate mitochondria. **B** Quantitative analysis of single mitochondrial perimeter in hippocampal neurons after AAVs injection (n = 20 mitochondrial/group). **C, D** Representative immunoblotting bands (**C**) and relative expression (**D**) of mitochondrial dynamics (OPA1, MFN2, Drp1, Fis1) and mitochondrial biogenesis (PGC1 $\alpha$ , Nrf1) related proteins in hippocampus after AAVs injection (n = 4). **E** Representative images of mitochondrial ROS in the hippocampal DG region measured by MitoSOX Red staining (Scale bar is 20  $\mu$ m). Nuclei were stained in blue (DAPI). **F** Quantitative analysis of MitoSOX Red staining (n = 4). **G** Levels of ATP in each group after AAVs injection (n = 3). **H–J** Levels of oxidative stress related indicators (SOD, GSH, MDA) (n = 4). All data represent means  $\pm$  SEMs. \*, Comparison between C57 + AAV-vehicle and 5xFAD + AAV-vehicle group, \* $p < 0.05$ ; \*\* $p < 0.01$ ; \*\*\* $p < 0.001$ . #, Comparison between 5xFAD + AAV-vehicle and 5xFAD + AAV-MST1 group, # $p < 0.05$ ; ## $p < 0.01$ ; ### $p < 0.001$

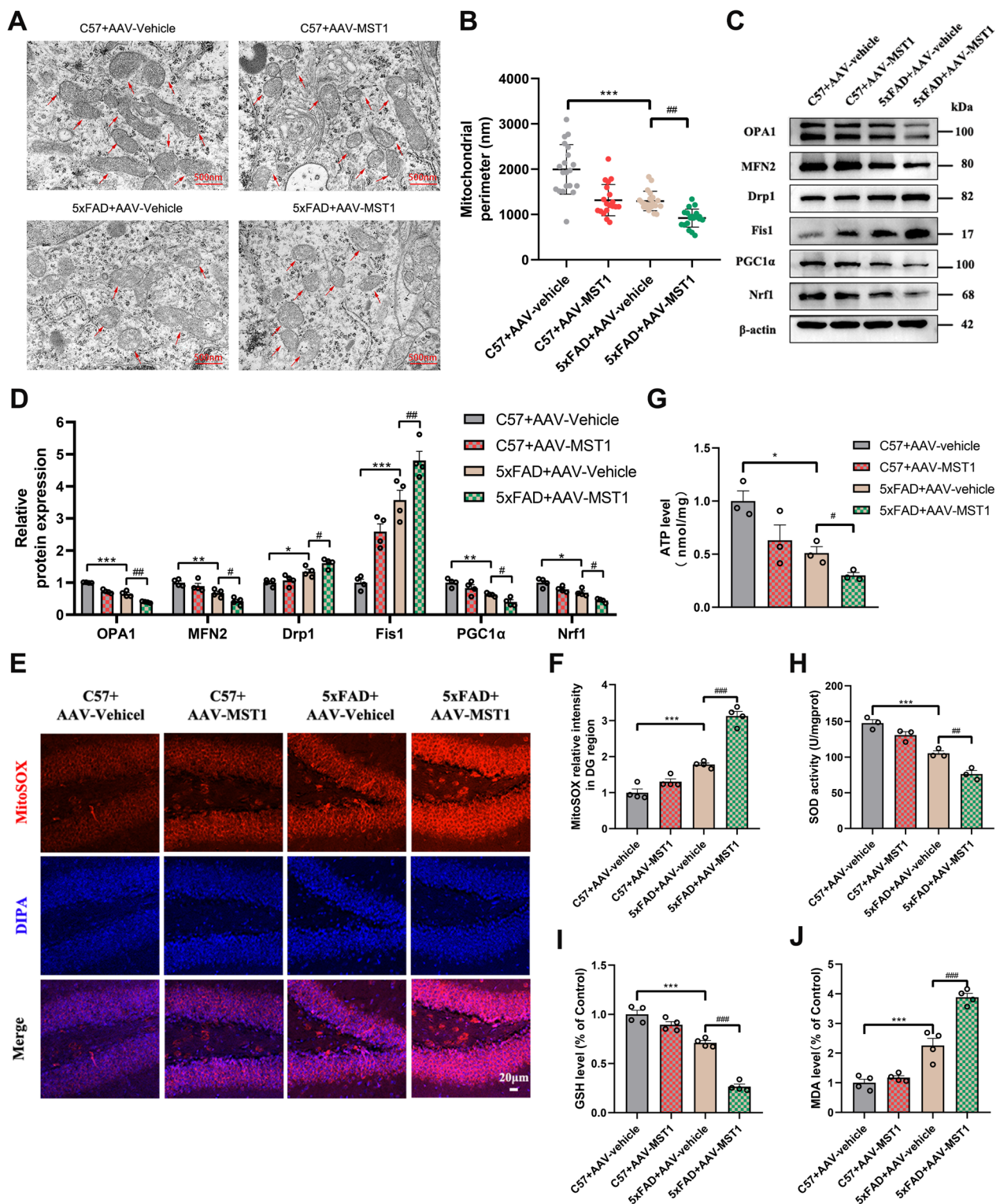


**Fig. 4** (See legend on previous page.)

showed a reduction in mitochondrial ROS levels following MST1 downregulation (Fig. 5L, M and Fig. S2D, E).

**Transcriptomic analysis of the regulatory effects of MST1 in 8-month-old 5xFAD mice**

To elucidate the molecular mechanism

underlying MST1's effect on AD, RNA-seq technology was employed. Transcriptome sequencing was conducted on hippocampal tissues from mice in the 5xFAD + AAV-vehicle and 5xFAD + AAV-shMST1 groups. The volcano plot displays the upregulated and downregulated genes within the differentially expressed genes (DEGs) (Fig. S3A). Overall, 359 DEGs ( $p \leq 0.01$ ) were assessed, with 162 downregulated ( $\log_2FC \leq -0.5$ ) and 197 upregulated ( $\log_2FC \geq 1.0$ ). The heatmap presents the DEG clustering analysis results, revealing the expression of an identical gene across various samples and confirming biological replicate consistency (Fig. 6A). The Venn diagram illustrates the gene counts detected in each group, while overlapping areas indicate co-expressed genes between the two groups (Fig. 6B). To elucidate the functional roles of the identified DEGs, Gene Ontology (GO) enrichment analyses and Kyoto Encyclopedia of Genes and Genomes (KEGG) pathway analyses were performed. GO enrichment of DEGs was primarily associated with cellular metabolism (NAD(P)+ nucleosidase activity, NAD+ nucleotidase, cyclic ADP-ribose generation, NAD+ nucleosidase activity) and immune inflammation regulation (positive regulation of immune effector processes, negative regulation of immune system processes, interleukin-6 production, and regulation of immune effector processes) (Fig. S3B). KEGG analysis revealed a significant enrichment of unigenes encoding enzymes in the oxidative phosphorylation pathway, with the PI3K-Akt signaling pathway the most significantly enriched (Fig. 6C). Enrichment was also observed in antioxidant resistance and chemical carcinogenic ROS pathways. Representative GSEA results aligned with the KEGG pathway findings (Fig. 6D, E). Significant upregulation of mitochondrial respiratory chain-related genes was observed following MST1 knockdown, including NADH dehydrogenase subunit 4 (*MT-ND4L*), ATP synthase F0 subunit 6 (*MT-ATP6*), cytochrome b oxidase (*MT-CO2*),

ATP synthase F0 subunit 8 (*MT-ATP8*), *Gm28439*, and *BC002163* (Fig. S3C).

#### MST1 effects on SH-SY5Y cell model induced by $\beta$ -amyloid in vitro

To investigate the effects and potential mechanisms of MST1 on cell models, SH-SY5Y cells were induced by  $A\beta_{1-42}$  as the AD in vitro model. Following treatment of SH-SY5Y cells with various concentrations of  $A\beta_{1-42}$  (0, 5, 10, 20, 40  $\mu$ M) for 24 h, WB results revealed that the level of MST1 activation (p-MST1) and the ratio of phosphorylated MST1 to total MST1 (p-MST1/MST1) gradually increased in a concentration-dependent manner. Given that statistical significance was achieved following 20  $\mu$ M  $A\beta_{1-42}$  exposure (Fig. 7A, B), this concentration was selected for subsequent experiments to establish the cell model. MST1 activation was assessed in the model and control groups using IF.  $A\beta$  caused a significant increase in the fluorescence intensity of p-MST1, consistent with the WB results (Fig. 7C, D).

Additionally, an MST1 overexpression plasmid and MST1-specific small interfering RNA (siRNA) were constructed, along with their respective vehicles, for cell transfection. WB and RT-qPCR results showed successful upregulation (Fig. S4A–C) or downregulation (Fig. S4D–F) of MST1, respectively. Additionally, CCK8 assay results revealed a decrease in SH-SY5Y cell viability upon treatment with  $A\beta_{1-42}$ . Moreover, MST1 overexpression further reduced cell viability (Fig. 7E). However, loss of MST1 expression promoted cell survival (Fig. 7F). Additionally, the abundance of mitochondria-dependent apoptosis-related proteins (Bax, Cleaved Caspase 3, and Cyt-C) was increased in the AD cell model, with a more pronounced increase following transfection with the MST1 overexpression plasmid (Fig. S4G, H). However, transfection with siRNA reversed this effect (Fig. S4I, J). The trend in the antiapoptotic protein Bcl-2 abundance was opposite to that of the apoptotic proteins in

(See figure on next page.)

**Fig. 5** MST1 Knockdown alleviates cognitive impairment and mitochondrial damage in 8-month 5xFAD mice. **A** Schematic of experimental proposition in vivo. AAV-GFP-vehicle and AAV-GFP-shMST1 were injected into the hippocampus of 7-month-old C57 mice and 5xFAD mice, and then the mice were divided into four groups: C57 + AAV-vehicle, C57 + AAV-shMST1, 5xFAD + AAV-vehicle, and 5xFAD + AAV-shMST1 for experiments. One month later, MWM test was performed, and finally all mice were euthanized for other experiments. **B** Western blotting was used to analyze the levels of hippocampus MST1 and p-MST1 after AAVs injection. **C** Quantitative analysis of MST1 and p-MST1 in hippocampus ( $n = 3$ ). **D** MST1 mRNA levels in the hippocampus after AAVs injection were detected using RT-qPCR ( $n = 3$ ). **E–I** MWM test results of four groups of mice, including swimming speed (**E**), escape latency (**F**), total time spent in the target quadrant (**G**), number of platform crossings (**H**), representative traces on fifth day the MWM training period (**I**). ( $n = 12$ /group). **J–K** Representative immunoblotting bands (**J**) and relative expression (**K**) of mitochondrial dynamics (OPA1, MFN2, Drp1, Fis1) and mitochondrial biogenesis (PGC1 $\alpha$ , Nrf1) related proteins in hippocampus after AAVs injection. **L** Representative images of mitochondrial ROS in the hippocampal DG region measured by MitoSOX Red staining (Scale bar is 20  $\mu$ m). Nuclei were stained in blue (DAPI). **M** Quantitative analysis of MitoSOX Red staining ( $n = 4$ ). All data represent means  $\pm$  SEMs. \*, Comparison between C57 + AAV-vehicle and 5xFAD + AAV-vehicle group, \* $p < 0.05$ , \*\* $p < 0.01$ , \*\*\* $p < 0.001$ . #, Comparison between 5xFAD + AAV-vehicle and 5xFAD + AAV-shMST1 group, # $p < 0.05$ ; ## $p < 0.01$ , ### $p < 0.001$

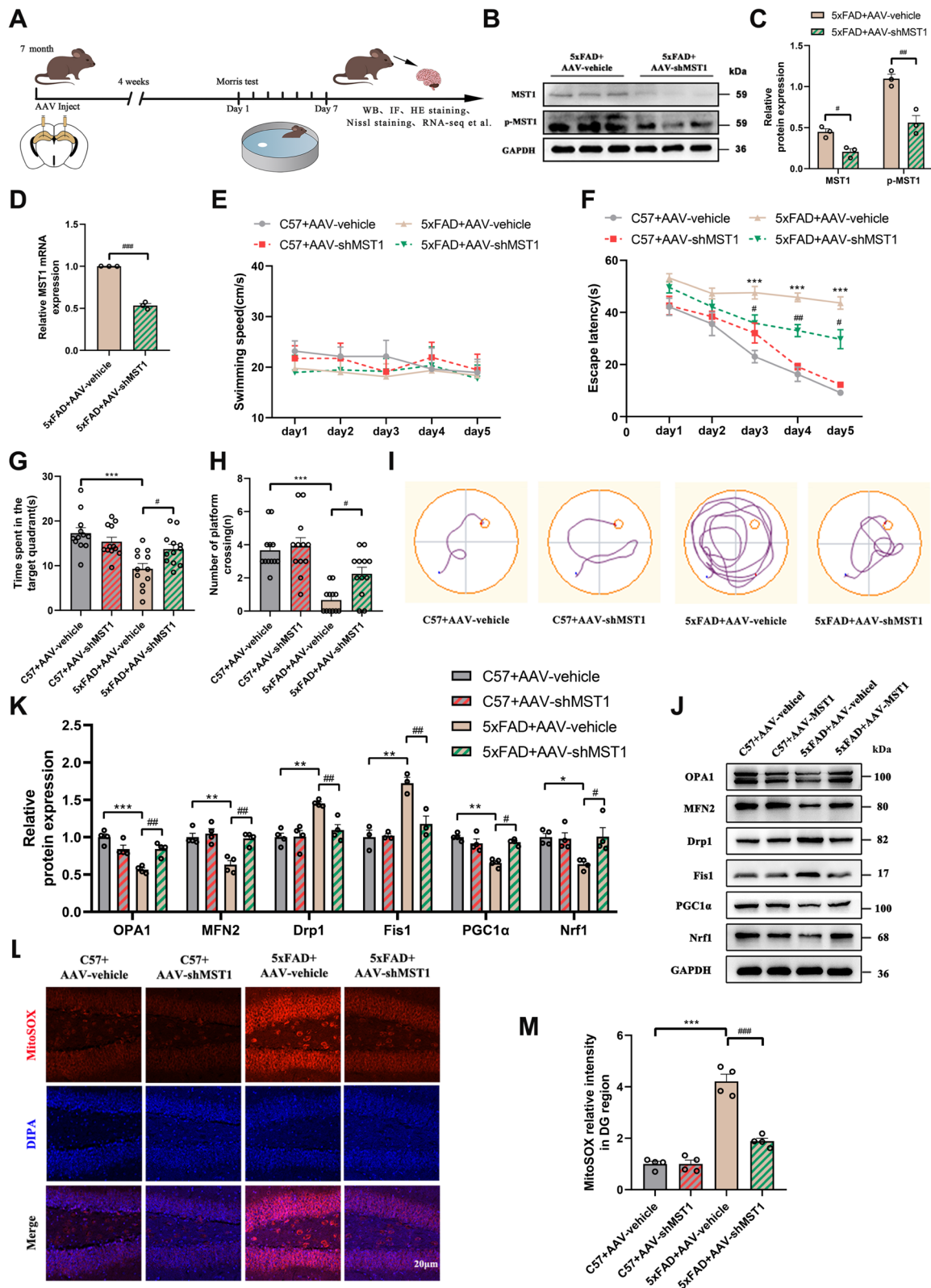


**Fig. 5** (See legend on previous page.)



each group (Fig. S4G–J). To further quantify the effect of MST1 on apoptosis, a flow cytometric analysis of apoptotic cells was performed. Increased apoptosis was observed in the A $\beta$  and ad-MST1+A $\beta$  groups compared with the control group. The apoptosis rate of the ad-MST1+A $\beta$  group was significantly higher than in the A $\beta$  group. Meanwhile, MST1 knockdown significantly decreased the apoptosis rate (Fig. 7G, H). These results indicate that MST1 was activated in A $\beta$ -treated cells, promoting SH-SY5Y cell apoptosis.

The effects of MST1 activation on mitochondrial morphology and function was also evaluated in SH-SY5Y cells. The MitoTracker staining data showed more mitochondrial fragmentation in the A $\beta$  and ad-MST1+A $\beta$  groups (Fig. S4K). Moreover, based on the TMRM and Mitosox Red staining results, the mitochondrial membrane potential decreased and mitochondrial ROS content increased in the ad-MST1+A $\beta$  group compared with the control and A $\beta$  groups, whereas MST1 knockdown reversed these manifestations (Fig. 7I–L). These findings support the potential of MST1 to regulate mitochondrial functions.

#### MST1 regulates the transcription of mitochondrial genes and affects mitochondrial oxidative phosphorylation by binding PGC1 $\alpha$

Following RNA-seq analysis, KEGG enrichment analysis was performed, identifying enrichment of the oxidative phosphorylation pathway. Among the DEGs, *MT-ND4L*, *MT-ATP6*, and *MT-CO2* differed significantly, all of which are associated with the oxidative phosphorylation pathway. To verify whether MST1 regulates mitochondrial gene transcription, the expression of these candidate genes was validated via RT-qPCR. The results showed a significant decrease in the mRNA expression of *MT-ND4L*, *MT-ATP6*, and *MT-CO2* in the ad-MST1+A $\beta$  group and a significant increase in the si-MST1+A $\beta$  group, compared with the A $\beta$  group (Fig. 8A, B). Additionally, the abundance of MT-ND4L, MT-ATP6 and MT-CO2 proteins was significantly decreased within the A $\beta$  and si-Ctrl+A $\beta$  groups, whereas knocking down MST1 effectively reversed this effect (Fig. S5A, B). Furthermore, upon overexpression of MST1, the abundance

of these proteins significantly decreased (Fig. S5C, D). These results suggest that MST1 modulates mitochondrial DNA transcription and the expression of ECT proteins in an AD cell model.

The subcellular localization of the activated form of p-MST1 at baseline was primarily concentrated in the cytoplasm and nucleus. However, in the AD cell model, the co-localization of p-MST1 and MitoTracker increased in the A $\beta$  group (Fig. 8C, D). This suggests that A $\beta$  treatment of SH-SY5Y cells promotes the activation of MST1 to the p-MST1 form and causes p-MST1 to accumulate on mitochondria.

To further explore the downstream molecular mechanism of MST1, Co-IP analyses were performed. PGC1 $\alpha$  was found to potentially bind to MST1 (Fig. 8E). PGC1 $\alpha$  is a key transcriptional co-activator that induces gene expression under physiological and pathological stress conditions. Moreover, a key function of PGC1 $\alpha$  is the activation of mitochondrial biosynthesis and oxidative phosphorylation [34]. Accordingly, we hypothesized that the effect of MST1 on mitochondrial oxidative phosphorylation-related genes involves PGC1 $\alpha$ .

WB and PCR experiments showed that the reduction in MT-ND4L, MT-ATP6, and MT-CO2 proteins and mRNA expression after MST1 overexpression was partially reversed by PGC1 $\alpha$  overexpression (Fig. 8F, G and Fig. S5E). Furthermore, MST1 overexpression reduced the maximum respiratory capacity and ATP production in cells while also increasing proton leakage within the ETC. However, overexpression of PGC1 $\alpha$  reversed the OCR impairment caused by MST1 (Fig. 8H–J). Additionally, the activity of mitochondrial respiratory chain complexes I–V was assessed. Overexpression of MST1 worsened the decline in complex enzyme activity induced by A $\beta$ ; PGC1 $\alpha$  overexpression mitigated this effect (Fig. 8K).

Taken together, these data support the notion that PGC1 $\alpha$  is an important downstream effector molecule of MST1, impacting mitochondrial oxidative phosphorylation in A $\beta$ -induced SH-SY5Y cells.

(See figure on next page.)

**Fig. 6** Exploring the Mechanisms of MST1 in Alzheimer's Disease through RNA-seq. The analysis of differentially expressed genes (DEGs) between 5xFAD + AAV-vehicle group and 5xFAD + AAV-shMST1 group. **A** Hierarchical clustering heatmap analysis of DEGs in each sample. The intensity of color represents the level of differentially expressed genes. Red indicates relatively high expression and blue represents relatively low expression. C1, C2, and C3 represent three samples of the 5xFAD + AAV-vehicle, M1, M2, and M3 represent three samples of the 5xFAD + AAV-shMST1. **B** Venn diagram of DEGs for two datasets. A total of 23776 co-expression genes were obtained. **C** Sankey diagram showing KEGG pathways enriched by DEGs. **D** GSEA plot of the Oxidative phosphorylation pathway.  $p < 0.05$ ,  $p\text{-adjust} < 0.05$ . **E** GSEA plot of the PI3K-Akt pathway  $p < 0.05$ ,  $p\text{-adjust} < 0.05$

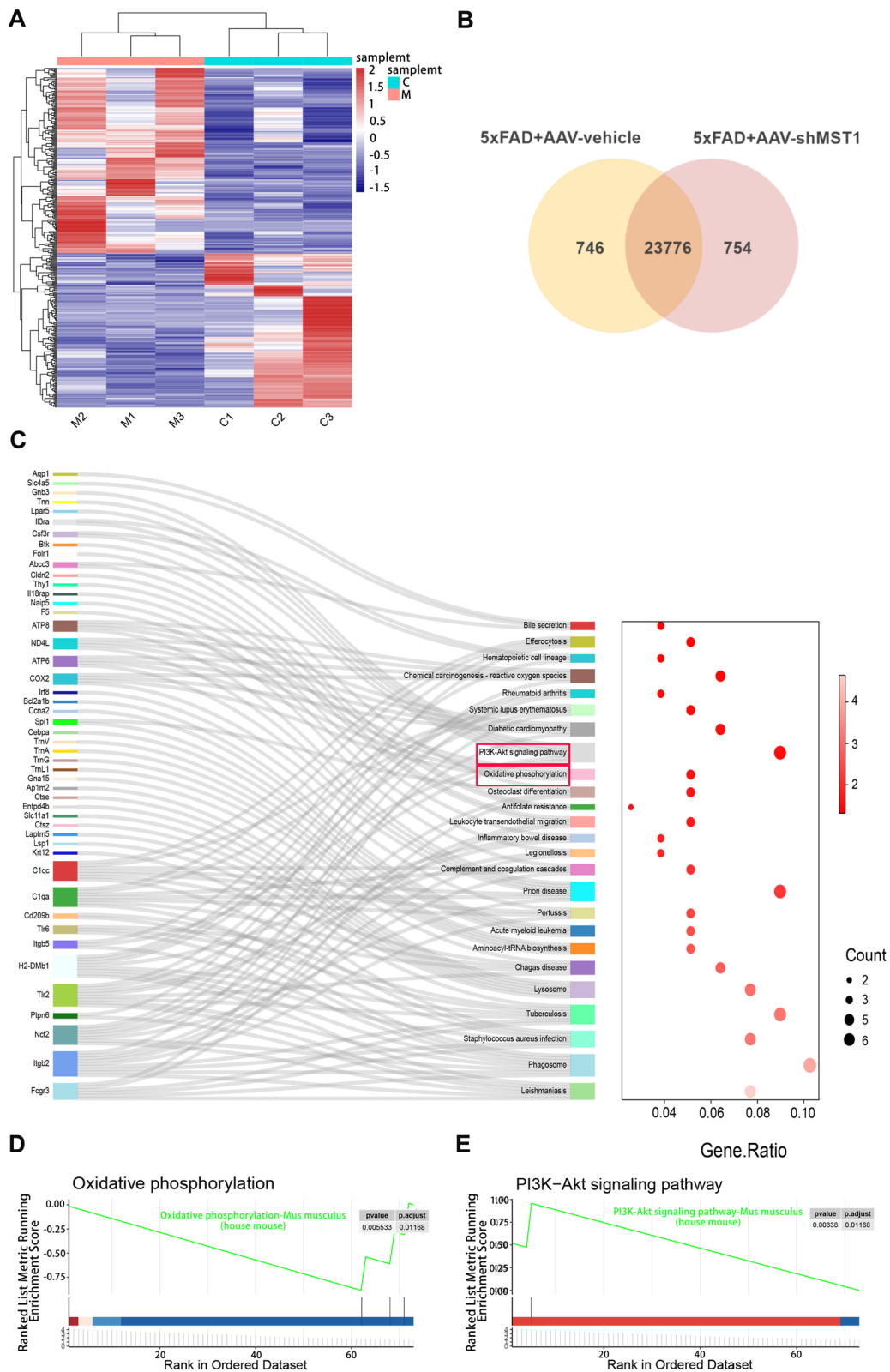


**Fig. 6** (See legend on previous page.)

### MST1 regulates oxidative stress through PI3K-Akt signaling in SH-SY5Y cells

Analysis of the RNA-seq results revealed enrichment of the PI3K-Akt pathway, suggesting its potential involvement in the effect of MST1 on AD regulation. To investigate the potential mechanism, changes in PI3K, Akt, and p-Akt protein expression was assessed upon upregulation or downregulation of MST1. WB revealed that p-Akt abundance was reduced in the A $\beta$  group and further decreased in the group overexpressing MST1 (Fig. 9A, B). However, the inhibitory effect observed in the A $\beta$  group was reversed when MST1 was knocked down (Fig. 9C, D). Total PI3K and Akt expression remained unchanged in all groups. To further evaluate the influence of the PI3K-Akt pathway on oxidative stress and mitochondrial function, MST1-overexpressing cells were treated with 740Y-P (25  $\mu$ M) for 24 h to activate the PI3K-Akt pathway. The expression of mitochondrial apoptosis proteins (Bax, Cleaved Caspase-3, and Cyt-C), initially induced by MST1 overexpression, was significantly reduced by 740Y-P. Hence, MST1-induced apoptosis was reduced by 740Y-P (Fig. 9A, B). Treatment of MST1-overexpressing cells with 740Y-P significantly suppressed ROS levels (Fig. 9E, F), facilitating MMP restoration (Fig. 9I, J).

Subsequently, MST1-knockdown cells were treated with LY294002 (20  $\mu$ M), a PI3K-Akt pathway inhibitor; the abundance of mitochondrial apoptosis-related proteins, namely Bax, Caspase-3, and Cyt-C, increased. In contrast, the antiapoptotic protein Bcl-2 was decreased in the si-MST1 + A $\beta$  + LY294002 group compared with the si-MST1 + A $\beta$  group (Fig. 9C, D). This indicates that the administration of LY294002 counteracted the protective effect of MST1 knockdown. Moreover, MST1 knockdown significantly alleviated oxidative stress and improved MMP compared with the A $\beta$  group, while LY294002 treatment exacerbated oxidative stress (Fig. 9G, H) and reduced MMP (Fig. 9K, L). These findings suggest that LY294002 reverses the inhibitory effects on oxidative stress and enhanced mitochondrial function induced by MST1 knockdown. Thus, as expected, MST1

might serve as a major regulator of the PI3K-Akt-ROS signaling pathway in A $\beta$ -induced SH-SY5Y cells.

### XMU-MP-1 relieves AD symptoms by inhibiting MST1 activity

XMU-MP-1—a novel Hippo kinase inhibitor—can effectively suppress MST1 expression [26]. Thus, 7-month-old WT and 5xFAD mice were intraperitoneally injected with XMU-MP-1 or DMSO for one month (Fig. 10A). The MWM results revealed significantly impaired spatial cognitive and memory abilities in the 8-month-old 5xFAD mice. However, following one month of treatment with XMU-MP-1, the 5xFAD mice exhibited shortened search times for hidden platforms, prolonged time spent in the target quadrant, and increased platform crossings (Fig. 10B–E). These results indicated that XMU-MP-1 rescued cognitive function impairments in 8-month-old 5xFAD mice.

Following one month of treatment, the abundance of certain proteins was evaluated via WB. The expression of p-MST1 was significantly suppressed, and p-MST1/MST1 levels decreased in the 5xFAD + XMU-MP-1 group (Fig. 10F, G). Moreover, synaptic-related proteins (PSD95 and SYP) were increased in the 5xFAD + XMU-MP-1 group compared with the 5xFAD + DMSO group (Fig. 10H, I). Levels of apoptosis-related proteins (Bax, Cleaved Caspase 9, Cleaved Caspase 3, and Cyt-C) decreased in the 5xFAD + XMU-MP-1 group (Fig. 10J, K). In contrast, the expression of the antiapoptotic protein Bcl-2 and mitochondrial biogenesis-related proteins (PGC1 $\alpha$  and Nrf1) increased in the 5xFAD + XMU-MP-1 group (Fig. 10J)–M). These results suggest that inhibiting MST1 expression through chemical methods yields effects consistent with gene knockout. Thus, blocking MST1 activation might improve cognitive and mitochondrial function, while reducing the incidence of mitochondrial apoptosis in 5xFAD mice.

Mechanistically, the abundance of mitochondrial respiratory chain-related proteins (MT-ND4L, MT-ATP6, and MT-CO2) was increased and the PI3K-Akt pathway

(See figure on next page.)

**Fig. 7** MST1 effects upon cell viability and mitochondria in vitro. **A, B** Western blotting measured the expression of MST1 and p-MST1 in SH-SY5Y cells cultured in 0, 5, 10, 20 and 40  $\mu$ M A $\beta$ 1-42 for 24 h. **B** Quantitative analysis of p-MST1/MST1 (n = 3). **C, D** Representative immunofluorescence images (C) and quantitative analysis (D) of p-MST1 in control and A $\beta$ -treated groups (Scale bar is 20  $\mu$ m). Nuclei were stained in blue (DAPI). (n = 3). **E** CCK8 assay was used to detect the cell viability of SH-SY5Y cells after treatment with A $\beta$ <sub>1-42</sub> or MST1 overexpressed plasmid. (n = 3) **F** CCK8 assay was used to detect the cell viability of SH-SY5Y cells after treatment with A $\beta$ <sub>1-42</sub> or MST1 specific siRNA (n = 3). **G, H** Flow cytometry analysis cells apoptosis of SH-SY5Y cells in different groups (Control, A $\beta$ , ad-MST1 + A $\beta$ , si-MST1 + A $\beta$ ). **I** Representative images of TMRM staining in SH-SY5Y cells in the Control, A $\beta$ , ad-MST1 + A $\beta$ , si-MST1 + A $\beta$  groups (Scale bar is 20  $\mu$ m). Nuclei were stained in blue (DAPI). **J** Quantitative analysis of TMRM. (n = 3). **K** Representative images of mitochondrial ROS in SH-SY5Y cells in the Control, A $\beta$ , ad-MST1 + A $\beta$ , si-MST1 + A $\beta$  groups measured by MitoSOX Red staining (Scale bar is 20  $\mu$ m). Nuclei were stained in blue (DAPI). **L** Quantitative analysis of MitoSOX Red staining (n = 3). All data represent means  $\pm$  SEMs. \*, Compared with the control group, \* $p$  < 0.05, \*\* $p$  < 0.01 and \*\*\* $p$  < 0.001. #, Comparison between intervention groups, # $p$  < 0.05; ## $p$  < 0.01

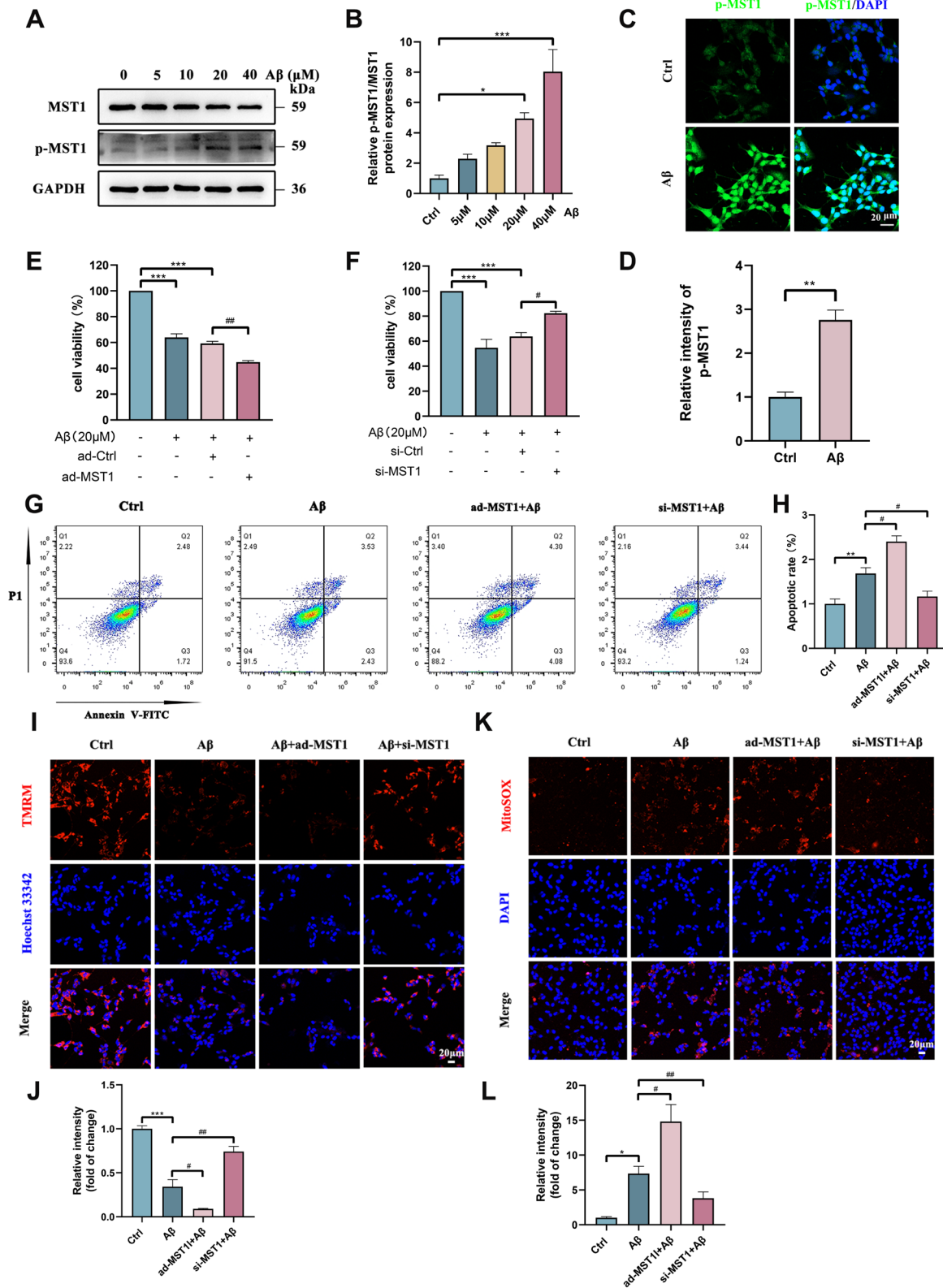


**Fig. 7** (See legend on previous page.)

became activated upon inhibition of MST1 activation by XMU-MP-1 (Fig. 10N–Q). This suggests that XMU-MP-1 affects mitochondrial gene expression and regulates the PI3K-Akt pathway in AD mice by inhibiting MST1.

## Discussion

Early AD is characterized by widespread mitochondrial dysfunction and oxidative damage [35, 36]. The mitochondrial genome is crucial to maintaining homeostasis [35, 37, 38]. Previous studies have reported proteomic analyses of various brain regions in patients with AD after death, revealing widespread dysregulation of the Hippo pathway in severely affected regions of the AD brain [15]. MST1, as the core kinase of the Hippo pathway, exhibits abnormal expression in the peripheral blood of patients with AD [39]. Notably, recent studies have shown that MST1 mediates neuronal loss and cognitive impairment in AD mice [14, 40]. In this study, we discovered that MST1 modulates mitochondrial DNA transcription (i.e., mitochondrial oxidative phosphorylation-related genes) and ROS levels to maintain mitochondrial homeostasis (Fig. 11). This regulatory process significantly influences cognitive impairment and neuronal damage in AD model mice, suggesting that MST1 could serve as a novel therapeutic target for AD.

Previous studies have highlighted that 5xFAD mice exhibit amyloid plaque deposition at an unusually early stage [41, 42]. In the current study, a significant quantity of amyloid plaques was also detected in mice as young as 3 months old, with steady accumulation as the mice aged. Moreover, a significant association was observed between MST1 activation and the pathological advancement of AD. The expression levels of p-MST1 in the hippocampus and cortex of 6-month-old 5xFAD mice were markedly higher than in WT mice. This underscores the activation of MST1 during amyloid-mediated neurodegeneration [14, 40]. Although many studies have focused on A $\beta$ -associated interventions, most related therapies have proven ineffective. Meanwhile, in the current study, MST1 activation similarly led to an AD-like phenotype

without increasing the burden of A $\beta$ . As indicated by previous research, the accumulation of A $\beta$  may not immediately lead to neurological damage, but the activation of MST1 can directly result in neuronal injury. Consequently, the relationship between MST1 activation and cognitive decline appears to be more closely correlated than that of A $\beta$  accumulation [40].

Information transmission between neurons occurs through synapses, which are crucial for maintaining normal physiological functions. Proteins such as PSD95 and SYP are pivotal in neuronal synapses, contributing to synapse formation and plasticity regulation. Meanwhile synaptic destruction serves as an early indicator of neuronal degeneration, with progressive neuronal and synaptic loss reflecting AD progression [43, 44]. According, MST1 was overexpressed in 4-month-old mice (early AD stage) and knocked down in 7-month-old mice (middle stage AD). Upregulation of MST1 exacerbated the AD phenotype and worsened neurodegeneration. This was evidenced by decreased spatial learning and memory, increased abundance of damaged and necrotic neurons, and impaired neuron synaptic plasticity. However, MST1 knockdown improved cognitive and neuronal functions and increased expression of synaptic proteins PSD95 and SYP, suggesting a reduction in synaptic loss. Similar results were observed following MST1 inhibition by XMU-MP-1 in 7-month-old mice. Overall, these findings confirm the involvement of MST1 in regulating cognitive, neuronal, and synaptic plasticity in AD.

Neurons, as high energy-demanding cells, depend on mitochondria as their energy factories. Within neurons are distinct structures, including cell bodies, dendrites, axons, and synapses, each with unique functions and specific requirements for mitochondrial storage pools [45, 46]. To sustain normal neuronal function, mitochondria must continually move, fuse, divide, and replicate, ensuring a dynamic balance. However, disruption in mitochondrial homeostasis can lead to neuronal damage [47]. While research on the relationship between MST1 and mitochondria in neurodegenerative diseases is relatively

(See figure on next page.)

**Fig. 8** MST1 regulates the mitochondrial genes expression by binding to PGC1 $\alpha$  in SH-SY5Y cell. According to the results of RNA-seq detection, three genes (MT-ND4L, MT-ATP6, MT-CO2) in the top 10 were selected for verification in A $\beta$ -treated SH-SY5Y cells. **A, B** Relative expression MT-ND4L mRNA, MT-ATP6 mRNA, and MT-CO2 mRNA after overexpression or knockdown of MST1 in AD cell models (n = 3). **C** Representative images showing co-localization of p-MST1 and MitoTracker (Scale bar is 10  $\mu$ m). (n = 3). Magnified image showing details of co-localisation (Scale bar is 5  $\mu$ m). **D** Co-localization analysis of p-MST1 and MitoTracker (n = 3). **E** Co-IP followed by western blot analyses confirmed the binding between MST1 and PGC1 $\alpha$  in the AD cell model. **F–H** Mitochondrial stress test analysis of oxygen consumption rate (OCR) in SH-SY5Y cells (n = 5) (**F**). Analysis of oxygen consumption rate (OCR), including basal respiration (**G**), proton leak (**G**), maximal respiration (**H**), ATP production (**H**). **I, J** Relative levels of MT-ND4L, MT-ATP6, and MT-CO2 protein in control, A $\beta$ , ad-MST1 + A $\beta$ , ad-MST1 + A $\beta$  + ad-PGC1 $\alpha$  group (n = 3). **K** Relative complex I-V enzyme activity in SH-SY5Y cells in the Control, A $\beta$ , ad-MST1 + A $\beta$ , ad-MST1 + A $\beta$  + ad-PGC1 $\alpha$  groups (n = 3). All data represent means  $\pm$  SEMs. \*, Compared with the control group, \*\* $p < 0.01$ . #, Comparison between intervention groups, # $p < 0.05$ ; ## $p < 0.01$  and ### $p < 0.001$

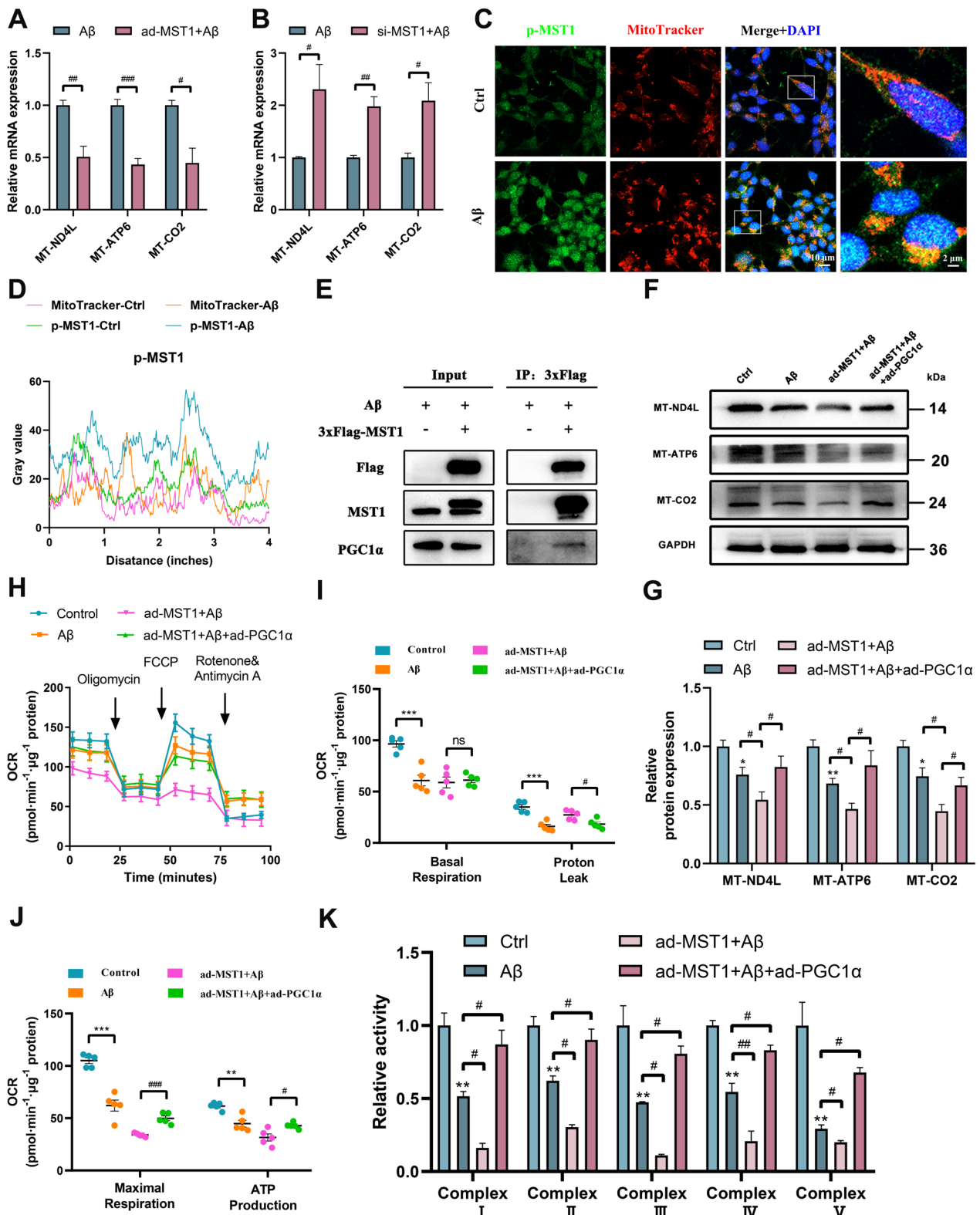


**Fig. 8** (See legend on previous page.)

limited, studies have examined how MST1 influences mitochondrial division, fusion, and autophagy processes through mitochondrial dynamic proteins [48, 49]. MST1 can induce alterations in mitochondrial ultrastructure, dysfunction, and ATP reduction in dilated cardiomyopathy [24], aligning with the current study's findings within the context of AD. Additionally, MST1 induces mitochondrial dysfunction by regulating mitochondrial ROS and oxidative stress [50, 51]. In the current study, Mito-SOX staining was performed to assess mitochondrial oxidative stress levels and SOD, GSH, and MDA levels were evaluated as indicators of intracellular oxidative stress. MST1 was found to modulate mitochondria and exacerbate cellular oxidative stress, consistent with previous findings.

Neuronal cell apoptosis, impaired synaptic plasticity, and mitochondrial dysfunction are important pathological features of AD. Mitochondria are vital for meeting the high energy demands of neuronal cells and synapses. Once mitochondrial homeostasis is disrupted in AD, neuronal apoptosis is induced and synaptic plasticity becomes impaired, ultimately leading to a progressive cognitive function decline. Collectively, the findings of this study reveal that MST1 activation disrupts mitochondrial homeostasis, causing mitochondrial damage-mediated neuronal apoptosis and synaptic plasticity impairment and exacerbating AD-like symptoms.

Assessing the influence of gene expression on signaling pathways provides insights into the significance of phenotypes, as the upregulation or downregulation of a single gene may have limited effects on complex phenotypes. In the current study, DEGs were analyzed in two datasets (5xFAD+AAV vehicle vs. 5xFAD+AAV shMST1) via GO, KEGG, and GSEA. Many DEGs were associated with cellular functions involving cellular energy metabolism and immune inflammation regulation. Similarly, previous studies have highlighted the influence of MST1 on cellular mitochondrial metabolism and oxidative stress [51], and its involvement in mammalian inflammation and regulation of innate and

adaptive immunity [52, 53]. Among the top DEGs were those belonging to the mitochondrial oxidative phosphorylation pathway, including *MT-ND4L*, *MT-ATP6*, and *MT-CO2*. The mitochondrial respiratory chain complex I, also known as nicotinamide adenine dinucleotide (NADH) dehydrogenase, serves as the entry point for electrons into the respiratory process. It is the largest protein complex, comprising 40 subunits. *MT-ND4L* is among the seven subunits encoded by mtDNA. Previous studies have linked *MT-ND4L* mutations and AD through whole-exome sequencing [54]. Moreover, a significant deficiency in complex I and IV enzymes has been reported in AD [55]. *MT-ATP6* is a subunit of mitochondrial complex V, contributing to mitochondrial ATP synthesis alongside proton transport. *MT-CO2*, a subunit of mitochondrial cytochrome c oxidase (Complex IV), plays a crucial role, and its impairment can result in mitochondrial respiratory chain dysfunction.

To further explore the role of MST1 on AD, the SH-SY5Y cell model was employed for in vitro assessment. Initially, concurrent activation of MST1 with increased A $\beta$  deposition was observed. This aligns with the in vivo results and further confirms the conclusions of previous studies [40]. Also consistent with the in vivo findings, MST1 influenced cell viability, facilitated apoptosis, and affected mitochondrial morphology and function.

Pathway analysis further revealed the influence of MST1 on various genes related to mitochondrial energy metabolism, particularly the mitochondrial respiratory chain-related genes *MT-ND4L*, *MT-CO2*, and *MT-ATP6*. The enrichment results were validated through RT-qPCR and WB. Mitochondria contain mtDNA, encoding 13 subunits of the OXPHOS system [56, 57]. Mitochondria primarily generate ATP through OXPHOS, highlighting the significance of regulating OXPHOS subunits for mitochondrial homeostasis. To further explore the downstream molecular mechanism of MST1, Co-IP experiments were performed, revealing that PGC1 $\alpha$  could potentially bind to MST1. PGC1 $\alpha$  is the primary regulatory factor for

(See figure on next page.)

**Fig. 9** MST1 affects oxidative stress through PI3K-Akt pathway, thereby affecting mitochondrial function. SH-SY5Y cells were incubated with 25  $\mu$ M of PI3K-Akt activator (740 Y-P) for 1 h before treatment with A $\beta$  after transfection with MST1 overexpression plasmid. SH-SY5Y cells were incubated with 20  $\mu$ M of PI3K-Akt Inhibitor (LY294002) for 1 h before treatment with A $\beta$  after transfection with MST1 specific siRNA. **A, B** Relative levels of PI3K, Akt, p-Akt, Bax, Bcl-2, Cleaved-Caspase 3, and Cyt-C protein in control, A $\beta$ , ad-MST1 + A $\beta$ , ad-MST1 + A $\beta$  + 740Y-P group (n = 3). **C, D** Relative levels of PI3K, Akt, p-Akt, Bax, Bcl-2, Cleaved-Caspase 3, and Cyt-C protein in control, A $\beta$ , si-MST1 + A $\beta$ , si-MST1 + A $\beta$  + LY294002 group (n = 3). **E–H** Relative intensity of ROS by Flow cytometry analysis in different groups. **I, J** Representative images (**I**) and quantitative analysis (**J**) of TMRM staining in SH-SY5Y cells in the Control, A $\beta$ , ad-MST1 + A $\beta$ , ad-MST1 + A $\beta$  + 740Y-P groups (Scale bar is 20  $\mu$ m). Nuclei were stained in blue (DAPI). (n = 3). **K, L** Representative images (**K**) and quantitative analysis (**L**) of TMRM staining in SH-SY5Y cells in the Control, A $\beta$ , ad-MST1 + A $\beta$ , si-MST1 + A $\beta$  + LY294002 groups (Scale bar is 20  $\mu$ m). Nuclei were stained in blue (DAPI). (n = 3). All data are repeated at least three times. All data represent means  $\pm$  SEMs. \*, Compared with the control group, \* $p$  < 0.05; \*\* $p$  < 0.01 and \*\*\* $p$  < 0.001. #, Comparison between intervention groups, # $p$  < 0.05; ## $p$  < 0.01 and ### $p$  < 0.001

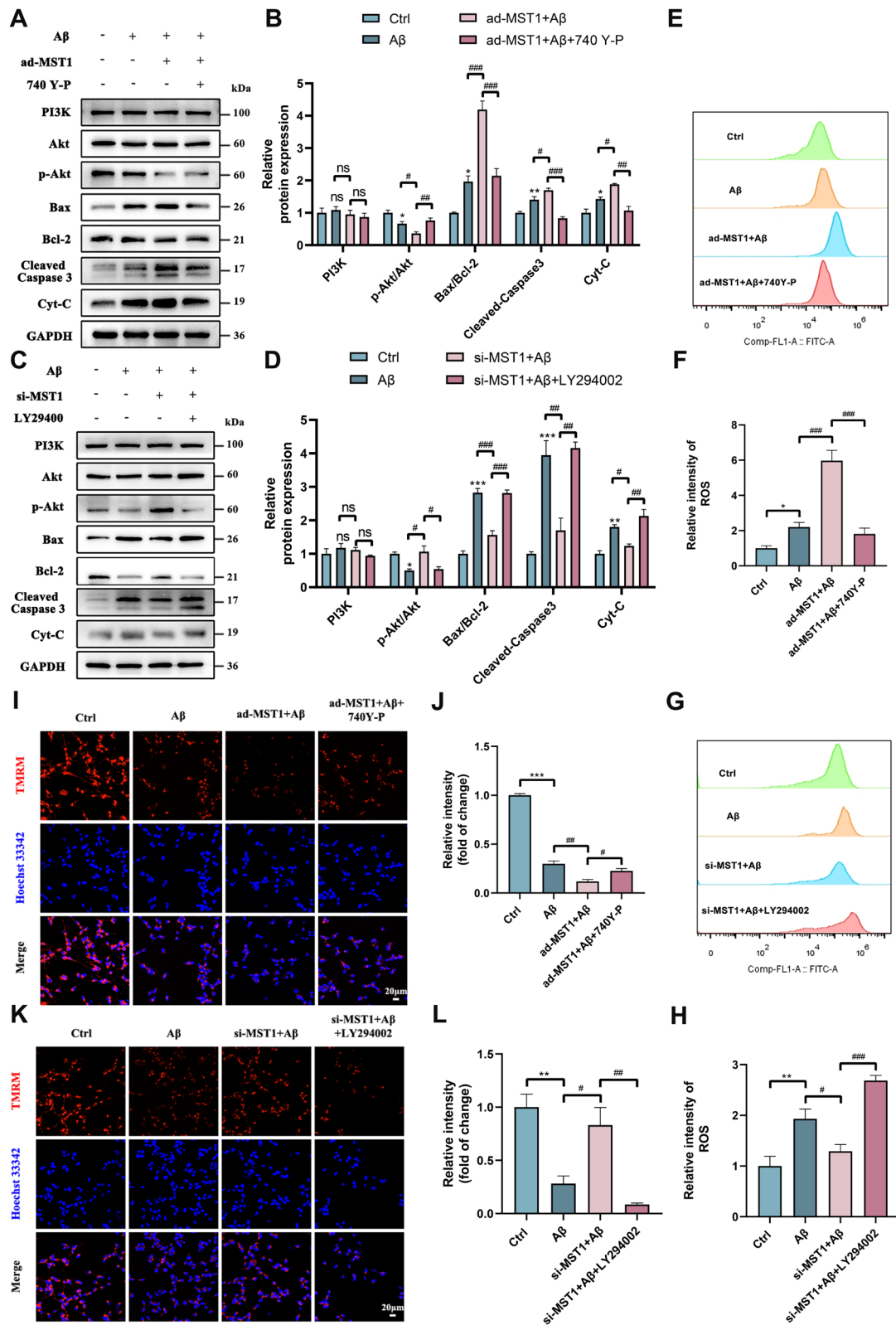


**Fig. 9** (See legend on previous page.)



mitochondrial biogenesis [57]. Its overexpression in myotubes enhances mtDNA levels and modulates its transcription [58]. PGC1 $\alpha$  can also stimulate mitochondrial respiration by inducing the expression of OXPHOS subunits [59]. Thus, to investigate whether the influence of MST1 on mtDNA transcription and related-protein expression is associated with downstream PGC1 $\alpha$ , WB analysis was performed to verify the effects elicited by PGC1 $\alpha$  on MST1 on downstream MT-ND4L, MT-CO2, and MT-ATP6 protein expression. In addition, the activity of the mitochondrial respiratory chain complexes I–V was evaluated. MST1 reduced the activity of the five mitochondrial respiratory chain complexes, increased proton leakage, reduced maximum respiratory capacity, and impair ATP production. However, PGC1 $\alpha$  appeared capable of mitigating the impairment of respiratory chain complex enzymes and mitochondrial respiration induced by MST1 overexpression in cells. Overall, we hypothesize that MST1 modulates the transcription and translation of MT-ND4L, MT-CO2, and MT-ATP6 through PGC1 $\alpha$ , influencing the OXPHOS pathway and disrupting mitochondrial homeostasis.

The PI3K-Akt signaling pathway ranked highest in the KEGG pathway analysis, suggesting its association with the role of MST1 in AD. The PI3K-Akt signaling pathway is crucial in regulating fundamental cellular processes and metabolism [60]. This pathway is involved in various mechanisms of AD, such as neuronal loss, inflammation, oxidative stress, and glucose metabolism [61]. Other studies have reported that PI3K-Akt signal transduction impacts mitochondrial aerobic respiration and exerts broad effects on oxidative stress [62]. In addition, PI3K-Akt activation directly stimulates NADPH oxidase (NOx) and promotes ROS production [62]. Several studies have suggested that the Hippo pathway negatively modulates Akt [63]. In this study, similar to previous studies, MST1 prompted elevated oxidative stress, heightened levels of mitochondria-related apoptotic proteins and mitochondrial dysfunction by suppressing the PI3K-Akt pathway. In addition, chemical inhibitors or activators targeting the PI3K-Akt pathway counteracted the effects of MST1

in various treatments, thus affecting oxidative stress and mitochondrial function. Collectively, these data support the involvement of MST1 in AD development through regulation of the PI3K-Akt-ROS pathway.

Finally, XMU-MP-1 was intraperitoneally injected in 7-month-old 5xFAD mice to inhibit MST1 expression. This intervention alleviated cognitive impairment in AD mice. WB validation revealed that chemically modulating MST1 expression reduced apoptosis and synaptic damage. Additionally, variations in the expression of PGC1 $\alpha$ , mtDNA-encoded proteins, and proteins involved in the PI3K-Akt pathway were observed. Furthermore, *in vivo* testing confirmed that MST1 indeed influences oxidative phosphorylation and PI3K-Akt pathway, aligning with the *in vitro* findings.

While this study explored a novel mechanism involving MST1 in AD, it has certain limitations. Although this study primarily focused on the impact of MST1 on mitochondrial function and oxidative stress in AD, exploring its immunoregulatory role could provide a more comprehensive understanding of its involvement in the disease. Investigating how MST1 influences immune responses, neuroinflammation, and microglial activation in AD models may uncover additional therapeutic targets.

Overall, the results of this study indicate that MST1 modulates the transcription and translation of mtDNA through PGC1 $\alpha$ , culminating in dysfunction of the mitochondrial respiratory chain. It enhances oxidative stress through the PI3K-Akt pathway. These mechanisms can ultimately disrupt mitochondrial homeostasis in AD, thus accelerating cognitive impairment and neuronal damage in 5xFAD mice.

## Conclusions

This study presents evidence supporting the potential therapeutic benefits of targeting MST1. Additionally, translating findings from preclinical models to clinical settings is essential for developing effective therapeutic strategies for AD. Future studies should explore the correlation between MST1 expression levels, mitochondrial dysfunction, and cognitive decline in human AD patients. Additionally, to study MST1 as a potential biomarker for

(See figure on next page.)

**Fig. 10** XMU-MP-1 improves cognitive and mitochondrial function in 8-month-old 5xFAD mice. **A** Schematic of experimental proposition *in vivo* after treatment XMU-MP-1. **B–E** MWM test results of four groups (C57 + DMSO, C57 + XMU-MP-1, 5xFAD + DMSO, 5xFAD + XMU-MP-1) of mice, including swimming speed (**B**), escape latency (**C**), total time spent in the target quadrant (**D**), Number of platform crossings (**E**). (n = 10/group). **F, G** Relative levels of MST1, p-MST1 protein in the hippocampus (n = 4). **H, I** Relative levels of PSD95, and SYP protein in the hippocampus (n = 4). **J, K** Relative levels of Bax, Bcl-2, Cleaved Caspase 3, Cleaved Caspase 9 protein in the hippocampus (n = 4). **L, M** Relative levels of Mitochondrial biogenic protein (PGC1 $\alpha$ , Nrf1) in the hippocampus (n = 4). **N, O** Relative levels of MT-ND4L, MT-ATP6, and MT-CO2 in the hippocampus (n = 4). **P, Q** Relative levels of PI3K, Akt, and p-Akt protein in the hippocampus (n = 4). All data represent means  $\pm$  SEMs. \*, Comparison between C57 + DMSO and 5xFAD + DMSO group, \* $p < 0.05$ ; \*\* $p < 0.01$  and \*\*\* $p < 0.001$ . #, Comparison between 5xFAD + DMSO and 5xFAD + XMU-MP-1 group, # $p < 0.05$ ; ### $p < 0.001$

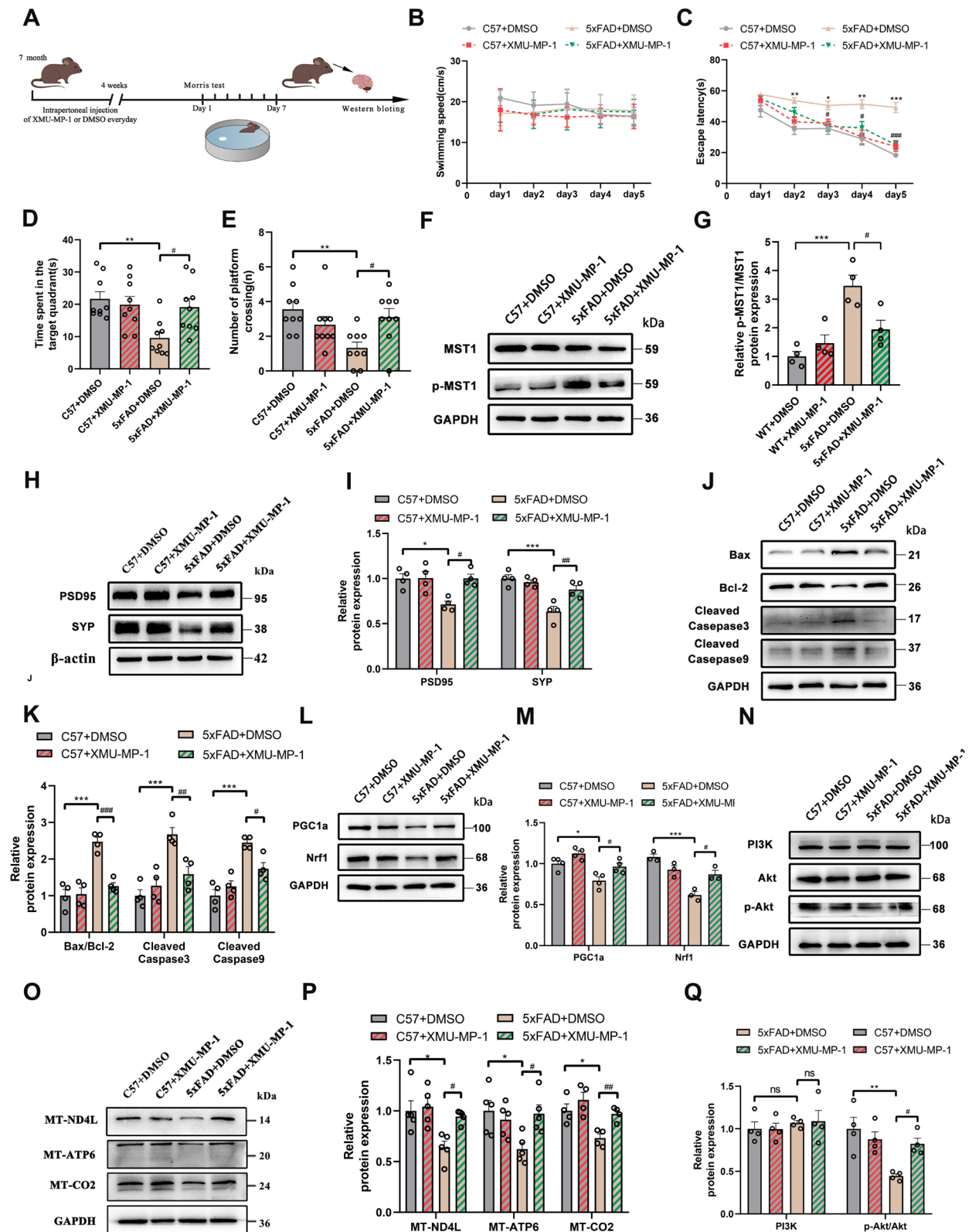


**Fig. 10** (See legend on previous page.)

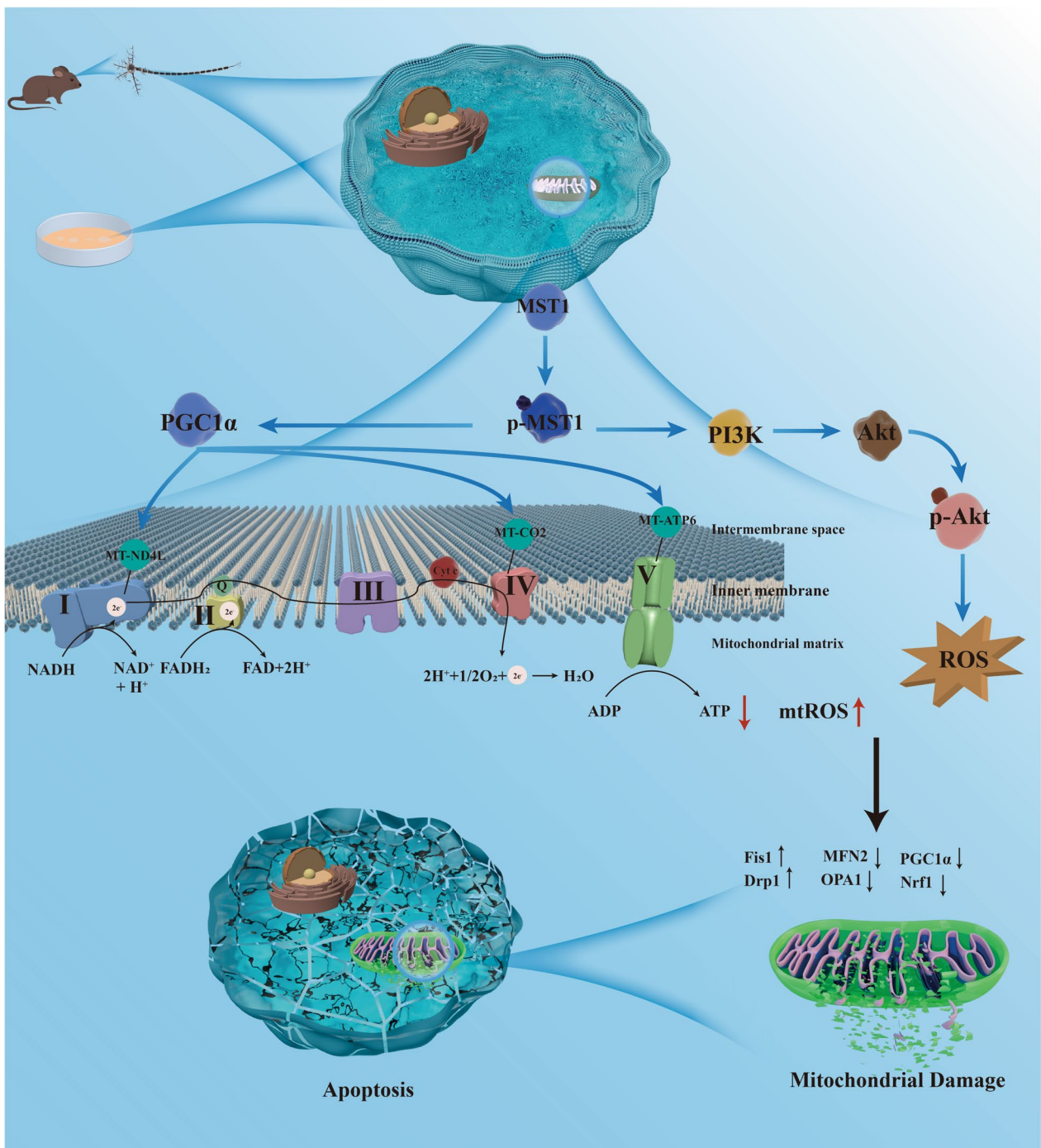


**Fig. 11** The underlying mechanism by which MST1 in Alzheimer's disease. MST1, participates in the progression of Alzheimer's disease, regulates mitochondrial homeostasis by mediating mitochondrial DNA transcription and the PI3K-Akt-ROS pathway

disease progression and therapeutic response, MST1 should be actively monitored and targeted in clinical trials for AD. This could ultimately help guide personalized treatment approaches for patients with AD.

#### Abbreviations

AAV	Adeno-associated virus
AD	Alzheimer's disease
A $\beta$	$\beta$ -Amyloid
ANOVA	Analysis of variance
BSA	Bovine serum albumin
CCK8	Cell-Counting-Kit-8
Co-IP	Co-Immunoprecipitation
DAB	Diaminobenzidine
DEG	Differently expressed gene
DRP1	Dynamin-related protein 1
ECL	Enhanced chemiluminescence
ECT	Electron transport chain
ELISA	Enzyme-linked immunosorbent assay
FCCP	Phenylhydrazine
FIS1	Fission 1 protein
HE	Hematoxylin–eosin
IF	Immunofluorescence
IHC	Immunohistochemistry
MFN2	Mitofusion 2
MWM	Morris water maze
MST1	Mammalian Ste20-like kinase
NRF1	Recombinant nuclear respiratory factor 1
OCR	Oxygen consumption rate
OCT	Optimal cutting temperature
OPA1	Optic atrophy 1
OXPHOS	Oxidative phosphorylation
PFA	Paraformaldehyde
PGC1 $\alpha$	Peroxisome-proliferator-activated $\gamma$ co-activator-1 $\alpha$
PSD95	Postsynaptic density-95
PVDF	Polyvinylidene difluoride
RIPA	Radio immunoprecipitation assay
ROS	Reactive oxygen species
SDS	Sodium dodecyl sulfate–polyacrylamide
SEM	Standard error of the mean
SYP	Synaptophysin
TEM	Transmission electron microscopy
WB	Western blotting

#### Supplementary Information

The online version contains supplementary material available at <https://doi.org/10.1186/s12967-024-05852-x>.

Supplementary material 1.

#### Acknowledgements

We would like to express our special thanks to Professor Fang Wang and Teacher Jing Han from the Animal Experiment Center of the Second Hospital of Shandong University for their assistance and guidance in animal experiments.

#### Author contributions

DC, PW, LC, and JB conceived and designed the research. DC, HL, XD, and DL performed the experiments. DC analyzed the data and drafted the manuscript. ZL and TW participated in RNA-seq data analysis and drafted relevant content for the manuscript. JB, PW, LC, SX, ZX, XZ, and HY are responsible for data supervision and manuscript review. All authors read and approved the final manuscript.

#### Funding

This study was supported by grants from the National Natural Science Foundation of China (82171410, 81870848), the Natural Science Foundation of

Shandong Provincial (ZR2023MH340), Cultivation Fund of the Second Hospital of Shandong University (2022YP93), Jinan Clinical Medical Science and Technology Innovation Program (202134018), Shandong University Multidisciplinary Research and Innovation Team of Young Scholars (2020QNQT019), and Clinical Research Center of Shandong University (No. 2020SDUCRCA001).

#### Availability of data and materials

The datasets supporting the conclusions of this article are available from the corresponding author upon reasonable request.

#### Declarations

##### Ethics approval and consent to participate

All animal procedures adhered to the National Institutes of Health Guide for the Care and Use of Laboratory Animals and received approval from the Ethics Committee of Shandong University Second Hospital (Approval No. KYLL2024362).

##### Consent for publication

Not applicable.

##### Competing interests

The authors declare that they have no competing interests.

##### Author details

<sup>1</sup>Department of Neurology, The Second Hospital of Shandong University, Shandong University, Jinan 250033, China. <sup>2</sup>Department of Neurology, Qilu Hospital of Shandong University, Jinan 250012, China. <sup>3</sup>The Second Hospital of Shandong University, Shandong University, Jinan 250033, China. <sup>4</sup>Department of Biomedical Engineering, School of Control Science and Engineering, Shandong University, Jinan 250061, China.

Received: 20 June 2024 Accepted: 31 October 2024

Published online: 22 November 2024

#### References

- Scheltens P, De Strooper B, Kivipelto M, Holstege H, Chételat G, Teunissen CE, et al. Alzheimer's disease. *Lancet*. 2021;397(10284):1577–90.
- Hardy JA, Higgins GA. Alzheimer's disease: the amyloid cascade hypothesis. *Science*. 1992;256(5054):184–5.
- Breijyeh Z, Karaman R. Comprehensive review on Alzheimer's disease: causes and treatment. *Molecules*. 2020;25(24):5789.
- Livingston G, Huntley J, Sommerlad A, Ames D, Ballard C, Banerjee S, et al. Dementia prevention, intervention, and care: 2020 report of the lancet commission. *Lancet*. 2020;396(10248):413–46.
- Reiss AB, Gulkarov S, Jacob B, Srivastava A, Pinkhasov A, Gomolin IH, et al. Mitochondria in Alzheimer's disease pathogenesis. *Life*. 2024;14(2):196.
- Harris Julia J, Jolivet R, Attwell D. Synaptic energy use and supply. *Neuron*. 2012;75(5):762–77.
- Dhapola R, Sarma P, Medhi B, Prakash A, Reddy DH. Recent advances in molecular pathways and therapeutic implications targeting mitochondrial dysfunction for Alzheimer's disease. *Mol Neurobiol*. 2021;59(1):535–55.
- Han Y, Liu D, Cheng Y, Ji Q, Liu M, Zhang B, Zhou S. Maintenance of mitochondrial homeostasis for Alzheimer's disease: strategies and challenges. *Redox Biol*. 2023;63:102734.
- Lee A, Kondapalli C, Virga DM, Lewis TL, Koo SY, Ashok A, et al. A $\beta$ 42 oligomers trigger synaptic loss through CAMKK2-AMPK-dependent effectors coordinating mitochondrial fission and mitophagy. *Nat Commun*. 2022. <https://doi.org/10.1038/s41467-022-32130-5>.
- Dhapola R, Beura SK, Sharma P, Singh SK, HariKrishnaReddy D. Oxidative stress in Alzheimer's disease: current knowledge of signaling pathways and therapeutics. *Mol Biol Rep*. 2024. <https://doi.org/10.1007/s11033-023-09021-z>.
- Morán M, Moreno-Lastres D, Marín-Buera L, Arenas J, Martín MA, Ugalde C. Mitochondrial respiratory chain dysfunction: implications in neurodegeneration. *Free Radical Biol Med*. 2012;53(3):595–609.

12. Alzheimer's Disease puzzle: delving into pathogenesis hypotheses. *Aging and disease*. 2024.
13. Lanzillotta C, Di Domenico F, Perluigi M, Butterfield DA. Targeting mitochondria in Alzheimer disease: rationale and perspectives. *CNS Drugs*. 2019;33(10):957–69.
14. Irwin M, Tare M, Singh A, Puli OR, Gogia N, Riccetti M, et al. A positive feedback loop of Hippo- and c-Jun-Amino-terminal kinase signaling pathways regulates amyloid-beta-mediated neurodegeneration. *Front Cell Dev Biol*. 2020. <https://doi.org/10.3389/fcell.2020.00117>.
15. Xu J, Patassini S, Rustogi N, Riba-Garcia I, Hale BD, Phillips AM, et al. Regional protein expression in human Alzheimer's brain correlates with disease severity. *Commun Biol*. 2019. <https://doi.org/10.1038/s42003-018-0254->.
16. Tasker R, Rowlands J, Ahmed Z, Di Pietro V. Co-expression network analysis of micro-rnas and proteins in the Alzheimer's brain: a systematic review of studies in the last 10 years. *Cells*. 2021;10(12):3479.
17. Sahu MR, Mondal AC. The emerging role of Hippo signaling in neurodegeneration. *J Neurosci Res*. 2019;98(5):796–814.
18. Meng Z, Moroishi T, Guan K-L. Mechanisms of Hippo pathway regulation. *Genes Dev*. 2016;30(1):1–17.
19. Yu L, Liu Y, Jin Y, Cao X, Chen J, Jin J, et al. Lentivirus-mediated HDAC3 inhibition attenuates oxidative stress in APP<sup>swe</sup>/PS1<sup>dE9</sup> mice. *J Alzheimers Dis*. 2018;61(4):1411–24.
20. Sanphui P, Biswas SC. FoxO3a is activated and executes neuron death via Bim in response to  $\beta$ -amyloid. *Cell Death Dis*. 2013;4(5):e625.
21. Li D, Ni H, Rui Q, Gao R, Chen G. Mst1: function and mechanism in brain and myocardial ischemia reperfusion injury. *Curr Neuropharmacol*. 2018;16(9):1358–64.
22. Jeong DJ, Um J-H, Kim YY, Shin DJ, Im S, Lee K-M, et al. The Mst1/2-BNIP3 axis is required for mitophagy induction and neuronal viability under mitochondrial stress. *Exp Mol Med*. 2024;56(3):674–85.
23. Zhang J, Sun L, Li W, Wang Y, Li X, Liu Y. Overexpression of macrophage stimulating 1 enhances the anti-tumor effects of IL-24 in esophageal cancer via inhibiting ERK-Mfn2 signaling-dependent mitophagy. *Biomed Pharmacother*. 2019;114:108844.
24. Wu W, Ziemann M, Huynh K, She G, Pang Z-D, Zhang Y, et al. Activation of Hippo signaling pathway mediates mitochondria dysfunction and dilated cardiomyopathy in mice. *Theranostics*. 2021;11(18):8993–9008.
25. Ma C, Fan L, Wang J, Hao L, He J. Hippo/Mst1 overexpression induces mitochondrial death in head and neck squamous cell carcinoma via activating  $\beta$ -catenin/Drp1 pathway. *Cell Stress Chaperones*. 2019;24(4):807–16.
26. Fan F, He Z, Kong LL, Chen Q, Yuan Q, Zhang S, et al. Pharmacological targeting of kinases MST1 and MST2 augments tissue repair and regeneration. *Sci Transl Med*. 2016;8(352):352ra108.
27. Yu L, Hu X, Xu R, Zhao Y, Xiong L, Ai J, et al. Piperine promotes PI3K/AKT/mTOR-mediated gut-brain autophagy to degrade  $\alpha$ -Synuclein in Parkinson's disease rats. *J Ethnopharmacol*. 2024;322:117628.
28. Takahashi S, Hisatsune A, Kurauchi Y, Seki T, Katsuki H. Insulin-like growth factor 1 specifically up-regulates expression of modifier subunit of glutamate-cysteine ligase and enhances glutathione synthesis in SH-SY5Y cells. *Eur J Pharmacol*. 2016;771:99–106.
29. Guo N, Soden ME, Herber C, Kim MT, Besnard A, Lin P, et al. Dentate granule cell recruitment of feedforward inhibition governs engram maintenance and remote memory generalization. *Nat Med*. 2018;24(4):438–49.
30. Bromley-Brits K, Deng Y, Song W. Morris water maze test for learning and memory deficits in Alzheimer's disease model mice. *J Vis Exp*. 2011. <https://doi.org/10.37971/2920>.
31. Sahu MR, Ahmad MH, Mondal AC. MST1 selective inhibitor Xmu-mp-1 ameliorates neuropathological changes in a rat model of sporadic Alzheimer's disease by modulating Hippo-Wnt signaling crosstalk. *Apoptosis*. 2024. <https://doi.org/10.1007/s10495-024-01975-0>.
32. Oakley H, Cole SL, Logan S, Maus E, Shao P, Craft J, et al. Intraneuronal  $\beta$ -amyloid aggregates, neurodegeneration, and neuron loss in transgenic mice with five familial Alzheimer's disease mutations: potential factors in amyloid plaque formation. *J Neurosci*. 2006;26(40):10129–40.
33. Lam J, Katti P, Biete M, Mungai M, AshShareef S, Neikirk K, et al. A universal approach to analyzing transmission electron microscopy with imageJ. *Cells*. 2021;10(9):2177.
34. Jannig PR, Dumesic PA, Spiegelman BM, Ruas JL. SnapShot: regulation and biology of PGC-1 $\alpha$ . *Cell*. 2022;185(8):1444.
35. Lin MT, Beal MF. Mitochondrial dysfunction and oxidative stress in neurodegenerative diseases. *Nature*. 2006;443(7113):787–95.
36. Weidling I, Swerdlow RH. Mitochondrial dysfunction and stress responses in Alzheimer's disease. *Biology*. 2019;8(2):39.
37. Shadel GS. Coupling the mitochondrial transcription machinery to human disease. *Trends Genet*. 2004;20(10):513–9.
38. Calame DG, Emrick LT. Functional genomics and small molecules in mitochondrial neurodevelopmental disorders. *Neurotherapeutics*. 2024;21(1):e00316.
39. Huo C, Chen M-H, Hour T-C, Huang L-C, Fong Y-O, Kuo Y-Y, et al. Application of micro-western array for identifying different serum protein expression profile among healthy control, Alzheimer's disease patients and patients' adult children. *Brain Sci*. 2022;12(9):1134.
40. Wang H, Shang Y, Wang E, Xu X, Zhang Q, Qian C, et al. MST1 mediates neuronal loss and cognitive deficits: a novel therapeutic target for Alzheimer's disease. *Progress Neurobiol*. 2022;214:102280.
41. Lee S, Jang KI, Lee H, Jo YS, Kwon D, Park G, et al. Multi-proteomic analyses of 5xFAD mice reveal new molecular signatures of early-stage Alzheimer's disease. *Aging Cell*. 2024. <https://doi.org/10.1111/ace1.14137>.
42. Korkmaz OT, Ay H, Aytan N, Carreras I, Kowall NW, Dedeoglu A, Tuncel N. Vasoactive intestinal peptide decreases  $\beta$ -amyloid accumulation and prevents brain atrophy in the 5xFAD mouse model of Alzheimer's disease. *J Mol Neurosci*. 2018;68(3):389–96.
43. Jack CR, Knopman DS, Jagust WJ, Petersen RC, Weiner MW, Aisen PS, et al. Tracking pathophysiological processes in Alzheimer's disease: an updated hypothetical model of dynamic biomarkers. *Lancet Neurol*. 2013;12(2):207–16.
44. Chang J, Li Y, Shan X, Chen X, Yan X, Liu J, Zhao L. Neural stem cells promote neuroplasticity: a promising therapeutic strategy for the treatment of Alzheimer's disease. *Neural Regen Res*. 2024;19(3):619–28.
45. Kiebish MA, Han X, Cheng H, Lunceford A, Clarke CF, Moon H, et al. Lipidomic analysis and electron transport chain activities in C57BL/6J mouse brain mitochondria. *J Neurochem*. 2008;106(1):299–312.
46. Stauch KL, Purnell PR, Fox HS. Quantitative proteomics of synaptic and nonsynaptic mitochondria: insights for synaptic mitochondrial vulnerability. *J Proteome Res*. 2014;13(5):2620–36.
47. Cardanho-Ramos C, Morais VA. Mitochondrial biogenesis in neurons: how and where. *Int J Mol Sci*. 2021;22(23):13059.
48. Shang H, VanDusseldorp TA, Ma R, Zhao Y, Cholewa J, Zanchi NE, Xia Z. Role of MST1 in the regulation of autophagy and mitophagy: implications for aging-related diseases. *J Physiol Biochem*. 2022;78(4):709–19.
49. Feng X, Wang S, Yang X, Lin J, Man W, Dong Y, et al. Mst1 knockout alleviates mitochondrial fission and mitigates left ventricular remodeling in the development of diabetic cardiomyopathy. *Front Cell Dev Biol*. 2021. <https://doi.org/10.3389/fcell.2020.628842>.
50. Wang P, Geng J, Gao J, Zhao H, Li J, Shi Y, et al. Macrophage achieves self-protection against oxidative stress-induced aging through the Mst-Nrf2 axis. *Nat Commun*. 2019. <https://doi.org/10.1038/s41467-019-08680-6>.
51. Wang Y, Yang Q, Shen S, Zhang L, Xiang Y, Weng X. Mst1 promotes mitochondrial dysfunction and apoptosis in oxidative stress-induced rheumatoid arthritis synoviocytes. *Aging*. 2020;12(16):16211–23.
52. Ueda Y, Kondo N, Kinashi T. MST1/2 balance immune activation and tolerance by orchestrating adhesion, transcription, and organelle dynamics in lymphocytes. *Front Immunol*. 2020. <https://doi.org/10.3389/fimmu.2020.00733>.
53. Li T, Wen Y, Lu Q, Hua S, Hou Y, Du X, et al. MST1/2 in inflammation and immunity. *Cell Adh Migr*. 2023;17(1):1–15.
54. Zhang X, Farrell JJ, Tong T, Hu J, Zhu C, Wang LS, et al. Association of mitochondrial variants and haplogroups identified by whole exome sequencing with Alzheimer's disease. *Alzheimers Dement*. 2021;18(2):294–306.
55. Holper L, Ben-Shachar D, Mann JJ. Multivariate meta-analyses of mitochondrial complex I and IV in major depressive disorder, bipolar disorder, schizophrenia, Alzheimer disease, and Parkinson disease. *Neuropsychopharmacology*. 2018;44(5):837–49.
56. Lim K. Mitochondrial genome editing: strategies, challenges, and applications. *BMB Rep*. 2024;57(1):19–29.
57. Kaariranta K, Uusitalo H, Blasiak J, Felszeghy S, Kannan R, Kauppinen A, et al. Mechanisms of mitochondrial dysfunction and their impact on age-related macular degeneration. *Prog Retin Eye Res*. 2020;79:100858.

58. Wu Z, Puigserver P, Andersson U, Zhang C, Adelmant G, Mootha V, et al. Mechanisms controlling mitochondrial biogenesis and respiration through the thermogenic coactivator PGC-1. *Cell*. 1999;98(1):115–24.
59. Lehman JJ, Barger PM, Kovacs A, Saffitz JE, Medeiros DM, Kelly DP. Peroxisome proliferator-activated receptor gamma coactivator-1 promotes cardiac mitochondrial biogenesis. *J Clin Invest*. 2000;106(7):847–56.
60. Chi M, Liu J, Mei C, Shi Y, Liu N, Jiang X, et al. TEAD4 functions as a prognostic biomarker and triggers EMT via PI3K/AKT pathway in bladder cancer. *J Exp Clin Cancer Res*. 2022. <https://doi.org/10.1186/s13046-022-02377-3>.
61. Kumar M, Bansal N. Implications of phosphoinositide 3-Kinase-Akt (PI3K-Akt) pathway in the pathogenesis of Alzheimer's disease. *Mol Neurobiol*. 2021;59(1):354–85.
62. Liu C-M, Ma J-Q, Sun Y-Z. Puerarin protects rat kidney from lead-induced apoptosis by modulating the PI3K/Akt/eNOS pathway. *Toxicol Appl Pharmacol*. 2012;258(3):330–42.
63. Ye X, Deng Y, Lai Z-C. Akt is negatively regulated by Hippo signaling for growth inhibition in *Drosophila*. *Dev Biol*. 2012;369(1):115–23.

### **Publisher's Note**

Springer Nature remains neutral with regard to jurisdictional claims in published maps and institutional affiliations.